



Constraining earthquake source inversions with GPS data: 2. A two-step approach to combine seismic and geodetic data sets

Susana Custódio,^{1,2} Morgan T. Page,^{3,4} and Ralph J. Archuleta^{1,5}

Received 14 April 2008; revised 28 October 2008; accepted 12 November 2008; published 27 January 2009.

[1] We present a new method to combine static and wavefield data to image earthquake ruptures. Our combined inversion is a two-step procedure, following the work of Hernandez et al. (1999), and takes into account the differences between the resolutions of the two data sets. The first step consists of an inversion of the static field, which yields a map of slip amplitude. This inversion exploits a special irregular grid that takes into account the resolution of the static data. The second step is an inversion of the radiated wavefield; it results in the determination of the time evolution of slip on the fault. In the second step, the slip amplitude is constrained to resemble the static slip amplitude map inferred from the GPS inversion. Using this combined inversion, we study the source process of the 2004 *M*₆ Parkfield, California, earthquake. We conclude that slip occurred in two main regions of the fault, each of which displayed distinct rupture behaviors. Slip initiated at the hypocenter with a very strong bilateral burst of energy. Here, slip was localized in a narrow area approximately 10 km long, the rupture velocity was very fast (≥ 3.5 km/s), and slip only lasted a short period of time (< 1 s). Then the rupture proceeded to a wider region 12–20 km northwest of the hypocenter. Here, the earthquake developed in a more moderated way: the rupture velocity slowed to ~ 3.0 km/s and slip lasted longer (1–2 s). The maximum slip amplitude was 0.45 m.

Citation: Custódio, S., M. T. Page, and R. J. Archuleta (2009), Constraining earthquake source inversions with GPS data: 2. A two-step approach to combine seismic and geodetic data sets, *J. Geophys. Res.*, *114*, B01315, doi:10.1029/2008JB005746.

1. Introduction

[2] Obtaining a reliable image of the evolution of slip during an earthquake is a longstanding goal of seismology. Accurate maps of faulting are essential to understanding the physics of earthquakes, and consequently to predicting the ground motion that may be expected from future earthquakes. The typical procedure to infer the evolution of slip on the fault is to solve a kinematic inverse problem, where records of ground motion are used to obtain the distribution of slip on the fault [e.g., Olson and Apsel, 1982; Hartzell and Helmberger, 1982]. The primary goal of kinematic inversions is to find a slip evolution that faithfully reproduces the observed ground motion. Even though kinematic faulting models do not provide a completely satisfying description of the earthquake source (these models are not required to obey the physical laws of rupture, and therefore

they may contain dynamical inconsistencies), they constitute an important starting point for most studies involving earthquake ruptures (e.g., studies of coseismic stress drops, dynamic modeling of earthquakes, studies of source scaling properties and frictional properties, prediction of ground motion for engineering purposes, studies of the Earth structure [e.g., Mikumo and Miyatake, 1995; Bouchon, 1997; Olsen et al., 1997; Ide and Takeo, 1997; Nielsen and Olsen, 2000; Somerville et al., 1999; Mai and Beroza, 2002; Favreau and Archuleta, 2003; Ma and Archuleta, 2006]).

[3] A complete kinematic model for faulting during an earthquake includes the time evolution of slip everywhere on the fault; that is, it consists of values of slip for every point on the fault at every time step. At any given time the ground motion is linearly related to the slip amplitude; thus, a faulting model can be obtained from the linear inversion of ground motion. However, a full space-time linear source inversion has an enormous number of unknowns (which is given by the number of points on the fault times the number of time steps) and without constraints the problem is actually ill-posed. Different methods have been devised to cope with the complexity of finite fault kinematic inverse problems. Olson and Apsel [1982] performed the first inversion for the evolution of faulting during an earthquake. They assumed that slip could occur in only five consecutive time windows of fixed length, centered about an average

¹Institute for Crustal Studies, University of California, Santa Barbara, California, USA.

²Now at Centro de Geofísica, Universidade de Coimbra, Coimbra, Portugal.

³U.S. Geological Survey, Pasadena, California, USA.

⁴Department of Physics, University of California, Santa Barbara, California, USA.

⁵Department of Earth Science, University of California, Santa Barbara, California, USA.

rupture velocity. This assumption largely decreased the number of free parameters in the inversion (compared to an inversion where all points on the fault are allowed to slip at any given time). They further found that physical and numerical constraints, no back-slip and pseudofiltering of small singular values, were required in order to obtain sensible solutions. This method, with small variations, of performing finite fault inversions (linear inversion, assuming that slip only occurs in a small number of consecutive time windows around a fixed average rupture velocity, imposing smoothness and positivity constraints) has been extensively used in studies of the seismic source [e.g., *Hartzell and Heaton*, 1983; *Wald et al.*, 1991; *Wald and Heaton*, 1994; *Wald et al.*, 1996; *Sekiguchi et al.*, 2000]. In order to study the details of rupture velocity, *Beroza and Spudich* [1988] developed an iterative linearized inverse method that allowed slip to occur in only one time window but at a variable rupture time. They concluded that a strong trade-off exists between slip amplitude and rupture time for a single station. *Cohee and Beroza* [1994a, 1994b] compared inversions performed with two different methods: (1) a linearized iterative inversion, where slip could occur only in one time window, at a variable rupture time, and (2) a linear inversion, where slip could occur in any of three consecutive time windows centered about a fixed average rupture velocity. They concluded that multiwindow methods are better to study earthquakes in which the risetime varies strongly; in the remaining cases single-window methods are more stable, and better at recovering the true seismic moment and average rupture velocity. *Cohee and Beroza* [1994b] further noted that neither approach could correctly recover the details of rupture propagation unless the static slip amplitude was constrained by independent data. *Das and Kostrov* [1990] developed a stable linear inverse algorithm to infer the full space-time evolution of slip that required only a few constraints, causality (the average rupture velocity must be slower than the P wave speed), no back-slip (no slip in the reverse direction is allowed at any time and point), and seismic moment (the seismic moment must match that inferred from teleseismic observations). This method allows for the retrieval of the earthquakes' source time functions from the observed ground motion, and it has been applied to several earthquakes [e.g., *Das and Kostrov*, 1990, 1994; *Henry and Das*, 2002]. The resolution ability of this algorithm has been carefully studied by *Das et al.* [1996] and *Das and Suhadolc* [1996], among others.

[4] With the aim of studying the details of the temporal evolution of faulting, *Hartzell and Liu* [1996] performed the first nonlinear finite fault inversion of ground motion. They recognized that ground motion is linearly related to the slip amplitude for a given rake angle, but nonlinearly related to the temporal rupture parameters, such as rupture velocity and risetime [*Archuleta*, 1984]. *Hartzell and Liu* [1996] successfully inferred the rupture history of the 1992 Landers, California, earthquake using a hybrid nonlinear algorithm that combined simulated annealing and downhill simplex features. They assumed that slip occurred in a single time window, obeying a prescribed source time function. Because nonlinear inversion algorithms have the ability to adequately explore the whole parameter space and yield a complete characterization of the earthquake source,

they have become the standard for finite fault inversions [e.g., *Hartzell et al.*, 1996; *Ji et al.*, 2002b; *Liu and Archuleta*, 2004; *Emolo and Zollo*, 2005; *Konca et al.*, 2007; *Piatanesi et al.*, 2007]. One of the major drawbacks of these nonlinear algorithms is that there is no clear mathematical way to assess the errors associated with the solutions obtained. Furthermore, the solutions of the nonlinear inversions are not unique. Thus, after solving the kinematic nonlinear inverse problem, we are left with a solution (a model for the evolution of slip) that is not unique and whose error we cannot assess quantitatively.

[5] Because of advances in computing capabilities and mathematical tools, the last decades have witnessed important developments in kinematic source inversion procedures. Kinematic inversions for slip models are now performed almost routinely after moderate to large earthquakes. However, different studies often produce different kinematic models for the same earthquake; even the final slip distributions can be very different. This discrepancy in kinematic models results from different authors using different data sets as inputs to their inversions, as well as different methods and assumptions. The scientific community often fails to recognize these differences in the approaches. Instead, the scientific community focuses on the disagreement between the different slip models, often ignoring critical parameters such as rupture velocity and slip rate function. Careful studies of the errors associated with the kinematic faulting models are therefore of prime importance. Several authors have recently focused their efforts on devising ways to assess the uncertainty in finite fault models [e.g., *Liu et al.*, 2006; *Piatanesi et al.*, 2007; *Monelli and Mai*, 2008]. In this paper we continue this effort by investigating the integration of data sets with different resolving abilities in source inversions.

[6] The first step in assessing the errors in earthquake source models is to understand the resolution of the data sets utilized in the inversion. Kinematic inversions take as inputs two main types of data: (1) records of permanent ground deformation (static field), and (2) records of ground motion or shaking (radiated wavefield or dynamic field). The static field can be used to infer the cumulative (final) slip amplitude and rake; the wavefield allows the retrieval of the complete evolution of slip in time. The two types of data sample different frequencies of ground motion; therefore, they are useful to image slip that occurs over different timescales. The two data sets also have different resolution wavelengths; that is, they carry information about slip that occurs over different length scales. Records of the static and dynamic field complement each other, and they should be used together in inversions [*Cohee and Beroza*, 1994b; *Wald et al.*, 1996; *Hernandez et al.*, 1999; *Delouis et al.*, 2002; *Ji et al.*, 2002a, 2002b; *Piatanesi et al.*, 2007]. However, given the different resolutions of these two types of data, one must be very careful in combining them.

[7] In this paper we will combine both the static field and the dynamic wavefield generated by the 2004 $M_w 6$ Parkfield, California, earthquake in order to obtain a model of the evolution of coseismic slip. Despite being only a moderately sized event, the 2004 Parkfield earthquake was extremely well recorded in the near-source area [*Harris and Arrowsmith*, 2006]. In addition, the location of the fault is almost perfectly known, based on surface trace and

seismicity [Rymer *et al.*, 2006; Thurber *et al.*, 2006]. The three-dimensional material structure of the Parkfield region is also known with great detail [Thurber *et al.*, 2006]. Thus, the available Parkfield data sets provide a unique opportunity to study the limitations and abilities of inversion techniques [Custódio *et al.*, 2005; Hartzell *et al.*, 2007]. To infer the time-space evolution of slip, we will use records of ground displacement (13 Global Positioning System (GPS) coseismic offsets) and records of ground acceleration (43 strong motion accelerograms). One of the disadvantages of using the M_w 6.0 2004 Parkfield earthquake as a case study is that it was only a moderate-size earthquake. Therefore, the signal-to-noise ratio in some data is less than desirable. In particular, the overall low slip amplitude of the earthquake results in a weak static signal. Another disadvantage of this case study is that the GPS data set is limited in number of data, spatial coverage, and density. Finally, the Parkfield earthquake occurred along a section of the San Andreas Fault with a very complex fault zone structure. Because much of the data was recorded very close to or even in the fault zone, the source signal is often masked by phenomena that take place within the complex fault zone region. In all likelihood, most of these issues (low signal-to-noise ratio, complexity of the fault zone region) are pervasive in earthquake studies. Therefore, the Parkfield data sets should still provide a better-than-average representation of the data normally available for source inversions.

[8] The 2004 Parkfield earthquake was extensively studied shortly after its occurrence. In particular, different data sets and inversion methods were used to image the coseismic slip: Murray and Langbein [2006] inferred the slip-amplitude distribution from a linear inversion of GPS static offsets; Johanson *et al.* [2006] obtained jointly coseismic and postseismic slip from a combined linear inversion of GPS and Interferometric Synthetic Aperture Radar (InSAR); Langbein *et al.* [2006] used a combination of GPS (survey and campaign), electronic distance meter (EDM), and creepmeter data to estimate coseismic slip amplitude; Custódio *et al.* [2005] and Liu *et al.* [2006] used strong motion data in a nonlinear inversion to infer the slip amplitude, rake angle, rupture velocity and risetime; and Ji *et al.* [2004] used a selection of seismic and GPS data jointly in a nonlinear wavelet inversion to image slip amplitude, rake, rupture velocity and risetime.

[9] Why then perform yet another inversion for the source of the 2004 Parkfield earthquake? The main goal of this paper is to study how to combine different data sets, which contain complementary information but have different resolutions, in order to obtain a kinematic rupture model that is consistent with both GPS and seismic data and is as accurate and robust as possible. In doing so we will keep track of the errors associated with the data sets and faulting models whenever possible. Our combined inversion of the static and dynamic fields will be done in two steps, following the work of Hernandez *et al.* [1999]. In the first step we invert the GPS data to find the cumulative slip amplitude. The inversion of the GPS data is performed using an irregular grid that reflects the resolution wavelength of the static data. In the second step we invert the strong motion data to obtain the distributions of slip amplitude, rake, secant (or average) rupture velocity and risetime. In this second step, the slip amplitude is con-

strained to stay within the bounds determined by the static field inversion (using the irregular grid). This work improves on Hernandez *et al.*'s [1999] work by using the GPS information explicitly (considering data errors and model resolution) to constrain the strong motion inversion. This two-step procedure takes into account the resolution of the GPS data, and by doing so naturally reduces model error in the final solution. It also copes adequately with the nonlinear complexity of the waveform inversion, which leads to a better control of the temporal rupture parameters. For comparison, we also present rupture models based on the individual data sets (geodetic and seismic). Finally, we examine the robustness of our final space-time slip distribution. Given the robust features of our combined rupture model, we discuss the 2004 Parkfield earthquake in terms of source processes.

2. Data

[10] Static data and waveform data complement each other regarding the earthquake source information they contain. Static field data are position offsets; that is, they are observations of differences in ground positions before and after the earthquake and represent zero-frequency motion. Waveforms are records of the passage of seismic waves that contain frequencies greater than zero, but are limited by instrument response and signal to noise. In this paper we will use static offsets recorded by GPS sensors and acceleration waveforms recorded by strong motion sensors. We will not use InSAR data to study the coseismic slip because the InSAR records contain both coseismic and postseismic displacements (the 2004 Parkfield earthquake was followed by high-amplitude postseismic slip that began immediately after the earthquake [Johanson *et al.*, 2006]).

[11] GPS data are of great value to source inversions because they record ground displacements that occur on very long timescales corresponding to virtually 0 Hz. Consequently, GPS data are suited to image static slip on the fault. In contrast, seismic and other waveform data record higher-frequency ground motion. Thus, waveform data allow the study of slip on a fault that occurs over shorter periods of time. In general, high-frequency data (typically seismic data) are not sensitive to slow slip. One of the issues with static data concerns the sampling frequency of the ground positions. If the positions are not sampled frequently enough (e.g., if the measurement is a daily average), the inferred coseismic signal will most probably be contaminated with postseismic deformation. In fact, the term "coseismic GPS" traditionally refers to daily averages, which are not purely coseismic (this situation is changing with the advent of high rate GPS). On the other hand, waveforms, which are recorded at higher sampling rates, are always purely coseismic. The spatial resolutions of the static and dynamic field also differ. The static field decays as $1/r^2$, where r is the distance between the source (region where slip occurs) and the observation point (station) [Aki and Richards, 2002]. The dynamic wavefield decays only as $1/r$ [Aki and Richards, 2002]. Thus, static data deteriorate very quickly with distance from the source. Comparatively, waveform data have the potential for better resolution at larger distances. In particular, waveform data better resolve deep slip. Another difference

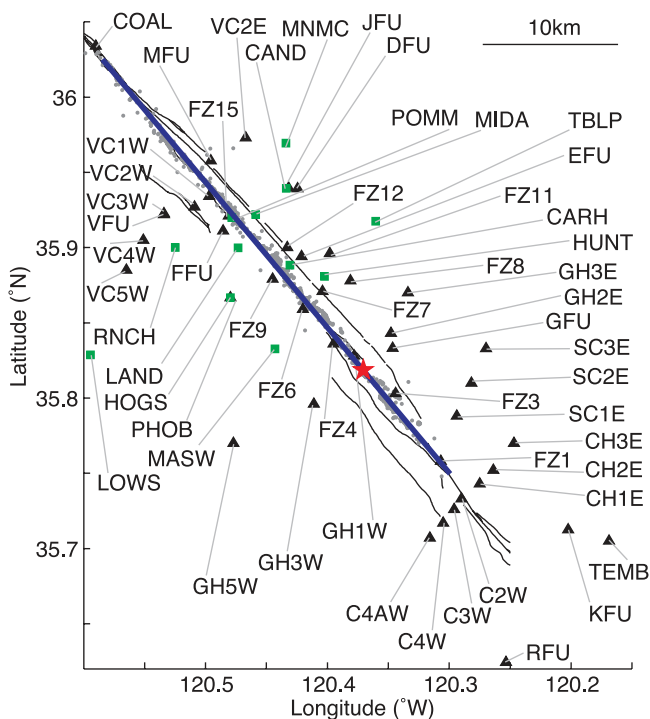


Figure 1. Map of the 43 strong motion stations (black triangles) and 13 GPS stations (green squares) used in this study. Also shown are San Andreas fault trace (black line) [Rymer *et al.*, 2006], aftershocks (gray dots) and epicenter (red star) of the 2004 Parkfield earthquake [Thurber *et al.*, 2006], and surface projection of the modeled fault plane (blue line).

in using static versus dynamic field data in source inversions is related to uncertainties in the material structure. Ground displacements are less sensitive to material structure than ground accelerations [Wald and Graves, 2001]. The models that we use for the media always contain inaccuracies and oversimplifications. Thus, it is advantageous to use records of the static field, which are more robust with respect to errors of the model used for the medium [Wald and Graves, 2001].

2.1. GPS Data

[12] The Global Positioning System records ground positions through a system of spaceborne satellites. In the Parkfield region, a network of 13 GPS stations (Figure 1) continuously records ground positions at a high sampling rate of 1 Hz [Langbein and Bock, 2004]. The ground positions that we use in this paper were obtained from Johnson *et al.* [2006]. The data processing follows Larson *et al.* [2003] with added modified sidereal filtering [Choi *et al.*, 2004]. The GPS data errors, as given by the data processing, are 1.49 mm for the east-west component, 2.97 mm for the north-south component, and 3.77 mm for the vertical component of displacement. The 1-Hz continuous GPS network at Parkfield recorded displacement waveforms during the 2004 event. However, in the specific case of the 2004 Parkfield earthquake, the 1-Hz sampling frequency of the GPS data is still too low to result in accurate waveforms [Page *et al.*, 2009]. Therefore, we only used GPS data to infer the coseismic static field; we did not

use GPS waveforms in the inversion. Because we infer the static displacements from 1-Hz GPS, we are confident that our static displacements are purely coseismic and do not contain any postseismic deformation. It is especially important to obtain truly coseismic offsets for the Parkfield earthquake given that strong postseismic deformation started immediately after the earthquake [Rymer *et al.*, 2006; Langbein *et al.*, 2006; Johanson *et al.*, 2006; Johnson *et al.*, 2006].

2.2. Strong Motion Data

[13] Strong motion accelerometers are seismographs designed to record strong ground shaking during earthquakes, they should stay on-scale even under high accelerations. Over 50 strong motion sensors recorded the 2004 Parkfield earthquake in the near-field [Shakal *et al.*, 2005, 2006; Borchardt *et al.*, 2006]. The strong motion data and processing methods that we use in this paper follow closely those employed by Liu *et al.* [2006]; hence we refer the reader to their paper for all details. Here, we will only overview the fundamental information concerning the data.

[14] We use accelerograms from 43 three-component strong motion stations. Figure 1 shows the location of the chosen stations [see Liu *et al.*, 2006, Table 1]. These 43 stations were chosen for quality reasons (proximity to epicenter, instrument response and clarity of the S phase). All 43 stations are located within 15 km of the presumed ruptured fault segment.

[15] Because some of the strong motion stations are located very close to or actually in the fault zone, the recorded ground motion contains signals that are modified by the complex fault zone (e.g., trapped waves, head waves and internal fault zone reflections [Ben-Zion, 1998]). In this paper, we do not attempt to model the effects of fault zone structure on wave propagation. Thus, for the purposes of our modeling, records that are obtained too close to the fault are contaminated by “noise” stemming from fault zone complexities. Furthermore, all stations are located on particular geological settings and these local conditions may affect the accelerations recorded during the earthquake. We assume that the distortion of the rupture source signal as recorded at each station is a result of site effects. In order to account for site effects, we use empirical factors that reflect the amplification and resonance of ground motion at each station [Liu *et al.*, 2006]. These empirical factors are based on ground motion recorded at the Parkfield strong motion network during the 1983 M_w 6.5 Coalinga earthquake. The Coalinga earthquake took place 25 km NE of Parkfield [Eberhart-Phillips, 1989].

[16] Before inverting the seismic data, we integrate the accelerograms into velocity waveforms. We further filter the waveforms in the passband 0.16–1 Hz, the accessible range of frequencies for the strong motion inversion [Liu *et al.*, 2006]. As an example, Figure 2 shows a velocity waveform obtained by integration of the recorded strong motion accelerogram. The same plot overlays nonfiltered and filtered velocity waveforms. Whereas the later parts of the filtered and nonfiltered signals almost overlap, there is some loss of detail in the earlier part of the filtered waveform. This indicates that some of the information carried by the seismic data will be left out of our study due to the limited frequency passband. Specifically, information contained in

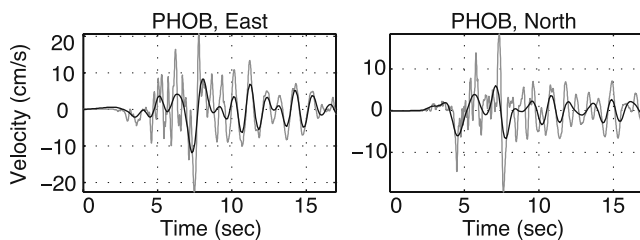


Figure 2. Horizontal components of ground motion recorded at strong motion station PHOB. The velocity waveforms were obtained by integration of the recorded accelerograms. Also shown in black is the strong motion velocity waveform filtered in the passband that we use in the inversion (0.16–1.0 Hz). Because we filter the seismic data in the passband 0.16–1.0 Hz, we are not able to image slip that occurs faster than 1 s (even though there is some evidence for faster slip in the raw data).

short-duration pulses will not be taken into account. Thus, we lose the ability to resolve the very fast slip that may have occurred during the earthquake. Given our passband, we will not be able to resolve slip occurring over periods of time shorter than 1.0 s.

[17] From this point onward we will refer to the velocity waveforms, obtained from the integration of accelerograms, filtered and corrected for site effects, as our seismic data or observations.

3. Methods

[18] The aim of source inversions is to find a rupture model that adequately describes an earthquake given the resulting ground motion. The adequacy of the inferred rupture model is normally assessed by comparing the observations (data) with the ground motion predicted by the model (synthetics). Thus, the solution of the inverse problem requires the computation of ground motion given prescribed rupture models. In other words, to address the inverse problem we must be able to adequately solve the corresponding forward problem. In order to solve the forward problem, we start by discretizing the fault plane into small subfaults. Next, we compute the Green’s functions for each pair: station and fault node (corner of a subfault). Green’s functions take into account the structure of the medium traversed by the seismic waves between the source (the point where slip occurred) and the observer (the station at the surface). The final ground motion predicted at a station is found by adding the contributions from all nodes on the fault. Once we know how to compute the ground motion that corresponds to any given slip distribution, we can focus on the inverse problem of finding the optimal rupture model that generates predictions (i.e., synthetic ground motion) that best match a set of observations. This procedure provides a measure of data fit (how well the data are matched) but does not specify model adequacy (how close to the true faulting solution the model actually is), which is more difficult to quantify for a nonlinear problem.

3.1. Fault Geometry and Material Structure

[19] We model the segment of the San Andreas Fault where the Parkfield earthquake took place as a subvertical

plane striking 140°SE and dipping 87°SW . The rupture plane dimensions are 40 km along strike and 13.65 km downdip. The geometry and location of the rupture plane were chosen in accordance with aftershocks locations (Figure 1) [Thurber *et al.*, 2006]. In previous studies we used rupture planes that extended deeper, but we found no significant deep slip [Custódio *et al.*, 2005; Liu *et al.*, 2006]. A fault plane that is larger than necessary adds dispensable free parameters to the inversion, which decreases its stability. Hence, we chose to limit the downdip width of the rupture plane to 13.65 km. We place the hypocenter at 35.8155°N , 120.3667°W and 8.3 km depth, in good agreement with its double-difference location [Thurber *et al.*, 2006]. Because the surface break during the Parkfield earthquake was minimal [Rymer *et al.*, 2006], we model a rupture plane that is buried 500 m below the surface. We discretize the rupture plane into nearly square subfaults that measure 2 km along strike and 1.95 km downdip.

[20] Following Liu *et al.* [2006], we approximate the complex 3D material structure as a layered structure that is different for each side of the fault [Liu *et al.*, 2006, Table 4]. This simplified velocity model takes into account the geologic differences between materials on opposite sides of the San Andreas Fault and allows the fast computation of Green’s functions. We apply the frequency-wave number method of Zhu and Rivera [2002] to compute the Green’s functions.

3.2. Inversion of Static Data

[21] Coseismic offsets are linearly related to slip on the fault. Therefore, it is possible to obtain the slip amplitude and rake from a linear inversion of the static field. Furthermore, because the inversion of the static data is a linear problem, we can calculate mathematically the resolution of the input data set and the error associated with the resulting slip model. Page *et al.* [2009] describe in detail the inversion of the GPS coseismic offsets of the 2004 Parkfield earthquake. Here, we briefly review their most important results. Page *et al.* [2009] start by demonstrating that a particular irregular gridding of the fault plane is required in order to retrieve the correct slip distribution from the inversion. Their irregular grid reflects the resolution wavelength of the static data. Because the static field strongly attenuates with distance between source and observer, slip that occurs over short length scales will be well resolved only if it happens near the GPS network. In such locations, we can discretize the fault into small subfaults and recover the correct slip. However, regions of the fault located far from GPS stations must be discretized coarsely in order to avoid artifacts in the solution [Sagiya and Thatcher, 1999; Pritchard *et al.*, 2002; Simons *et al.*, 2002]. This irregular gridding system is necessary to recover small-scale structure in well-resolved regions of the fault while simultaneously avoiding spurious structure, given the only 39 (13 stations \times 3 components) observations of coseismic offsets and the $1/r^2$ decay of the static field [Page *et al.*, 2009].

[22] Because kinematic inversions are often underdetermined problems, it is wise (and common practice) to improve their resolution with further knowledge of the physics of earthquakes. Such physical knowledge is built into the inversions in the form of constraints [e.g., Olson and Apsel, 1982; Hartzell and Heaton, 1983; Das and

Kostrov, 1990, 1994; *Das et al.*, 1996; *Das and Suhadolc*, 1996; *Hartzell and Liu*, 1996]. In their inversion of the static field, *Page et al.* [2009] impose a nonnegativity constraint (backslip is not allowed), as well as a seismic moment constraint. The nonnegativity constraint renders the static field inversion, which was initially a linear problem, nonlinear. Thus, *Page et al.* [2009] employ a nonnegative least squares (NNLS) algorithm [*Lawson and Hanson*, 1974] to perform the static field inversion. The moment constraint serves to avoid the appearance of spurious slip in the solution. *Page et al.* [2009] also assume that slip is purely right-lateral (rake angle = 180°), which is in accordance with previous results [*Custódio et al.*, 2005; *Liu et al.*, 2006; *Murray and Langbein*, 2006; *Johanson et al.*, 2006]. Fixing the rake angle reduces the number of free parameters by a factor of two, hence improving the resolution.

3.3. Inversion of the Wavefield

[23] We infer the space-time evolution of slip from the seismic data through a nonlinear simulated annealing inversion [*Hartzell and Liu*, 1996; *Liu and Archuleta*, 2004; *Liu et al.*, 2006]. Again, we will only review here the most important aspects of the inversion method; the more interested reader should refer to the original papers for further details. The inputs to the inversion are the seismic waveform data, the fault geometry, the Green's functions, and an assumed functional form of the slip rate function. The output of the inversion is a kinematic rupture model, which consists of the spatial distributions of slip amplitude, rake angle, secant rupture velocity (average rupture velocity between the hypocenter and each point on the fault) and accelerating and decelerating risetimes. The source slip rate function that we use is made up of two sinusoidal parts [*Liu et al.*, 2006]. Because we invert independently for accelerating and decelerating risetimes, the source slip rate function can be symmetric or asymmetric (to be determined by the data). The inversion algorithm of *Liu et al.* [2006] interpolates both the source parameters and the Green's functions to compute smooth synthetic ground motion. In this paper, source parameters are computed on a $2 \text{ km} \times 1.95 \text{ km}$ grid; Green's functions use a $0.5 \text{ km} \times 0.4875 \text{ km}$ grid, and both are interpolated and convolved on a finer $0.1667 \text{ km} \times 0.1625 \text{ km}$ grid (grid spacings are given first along strike, and then down dip).

[24] The goal of the inversion is to find optimal values for the five source parameters (slip amplitude, rake angle, rupture velocity, accelerating risetime and decelerating risetime) at every node on the fault. To achieve this goal, the algorithm performs a global search of the parameter space. This global search does not examine individually every possible rupture model. Instead, it samples a very large number of rupture models that provide a good representation of all the possibilities. For each examined rupture model, corresponding ground motion is computed and compared with data. The final rupture model is not necessarily the rupture model that generates ground motion that best fits the data, but rather a good representative of the family of models that best fit the data. In other words, our algorithm finds a good representation of the global minimum. The choice of sampled rupture models throughout the inversion is to some degree random (we do ensure that the entire parameter space is adequately sampled). This ran-

domness enables us to perform different inversions by taking different random paths; in this manner we can obtain different rupture models. The rupture models thus generated should all be equally good, they should all be good representatives of the global minimum of the parameter space and they should all predict ground motion that match the data. When we use this nonlinear inversion algorithm, we normally generate 10 equally good models from different random seeds. Because the 10 models are equally good (they produce nearly equal misfits between data and synthetics), we feel it would be misleading to present only one model. On the basis of the 10 models, we then compute an average rupture model and its standard deviation. The comparison of the 10 equally good models helps us analyze the robustness of our results. Note that the standard deviation of the 10 equally good models is a model error estimate that only takes into account the nonuniqueness of the inversion procedure. Data errors and uncertainties in the Green's functions, as well as other errors in the assumptions, are left out of this error estimate.

[25] The inversion of seismic data benefits from the inclusion of physically based constraints, just as the static field inversion does. We require that the seismic moment be as small as possible (in order to prevent spurious slip on the fault) and that the spatial distribution of slip be smooth. None of these constraints is imposed very strongly; the fit to the data is always the main priority.

3.4. Two-Step Combined Inversion

[26] Major uncertainties in the nonlinear seismic inversion stem from the trade-offs between the five source parameters. The areas where slip occurs can be mislocated in the rupture model if the rupture velocity and the risetime are not accurately determined, and vice versa [e.g., *Beroza and Spudich* 1988]. For example, for a given rupture velocity, slip will be located in a given region of the fault. But if the rupture velocity is faster, the inversion will put the slip farther away from the hypocenter. In other words, there is an intrinsic interdependence between temporal and spatial source parameters. A similar trade-off exists between rupture velocity and risetime. *Emolo and Zollo* [2005] concluded that the rupture velocity has a profound effect on any inversion result. In an attempt to overcome these trade-offs we follow the approach of *Hernandez et al.* [1999] and use the slip-amplitude distribution obtained from the static field inversion to guide the nonlinear seismic inversion. The combined inversion of static and waveform data is thus a two-step process. We diverge from *Hernandez et al.* [1999] in the linking of the two steps.

[27] The first step of the combined inversion is an inversion of the GPS static data only, which yields a map of coseismic slip amplitude. We assess the uncertainty associated with the static slip model by taking into account the observational errors of the GPS offsets. *Page et al.* [2009] describe in detail the process of inferring the error of the slip distribution from Monte Carlo error sampling. The main idea is to generate a large number of possible static data sets by adding to the static data small random perturbations within bounds given by the GPS errors (in this study we used 1000 data sets in the Monte Carlo sampling). All the data sets thus obtained are subsequently inverted to yield slip distributions. The standard deviation of all the slip

distributions gives a measure of the uncertainty in the slip model arising from data errors. In summary, the first step of the combined inversion consists of inferring a map of coseismic slip amplitude and respective error (as inferred from observation errors) from the static data. In order to take into account the resolution wavelength of the static data, all the static analysis is performed on the irregular grid proposed by *Page et al.* [2009].

[28] In the second step of the combined inversion, we invert the strong motion data under the constraint that the slip-amplitude distribution resembles that inferred from the static field (step one). Fixing the distribution of the slip amplitude in the seismic nonlinear inversion leads to a natural consolidation of the time source parameters [*Cohee and Beroza*, 1994b; *Hernandez et al.*, 1999]. In other words, using the static slip amplitude as a constraint on the seismic nonlinear inversion dramatically reduces the undesirable trade-offs between source parameters. The strong motion inversion is performed using a fault plane discretized into a regular grid (2 km \times 1.95 km). However, the slip distribution inferred from the GPS offsets was obtained on an irregular grid. In order to combine the two inversions, we must carefully consider the two gridded systems.

[29] The GPS-inferred static slip amplitude for each irregular subfault is the average slip that occurs within that subfault. Therefore, a natural way of combining the GPS and seismic inversions would be to require that in the second step (seismic inversion) the average slip within each irregular GPS subfault equals the GPS-inferred slip. This approach would be moment-conserving (the seismic moment would be identical in the two steps of the combined inversion). However, there is a problem with this reasoning: Because of the fast decay of the static field, slip placed at shallower depths within a large irregular subfault will create a larger GPS signal than the same amount of slip placed deeper within the subfault. In order to overcome this problem, in the second step (seismic inversion) we compute a weighted average of the slip amplitude within each irregular GPS subfault, rather than a simple average. The weight ascribed to the i th subfault on the regular grid, that is within the j th irregular subfault, is given by

$$w_i = \frac{\|b_i\|}{\|b_j\|}, \quad (1)$$

where $\|b_i\|$ is the L_2 norm of the GPS data vector generated by a unit of slip on the i th subfault. The GPS constraint is then given by

$$\sum_i w_i \Delta u_i = \tilde{x}_j, \quad (2)$$

which sums over the regular subfaults within each irregular subfault from the GPS inversion. Here Δu_i is the total slip on the i th regular subfault in the combined inversion, and \tilde{x}_j is the slip placed on the j th irregular subfault in the GPS inversion.

[30] Deeper subfaults have slightly smaller weights than shallower ones; therefore, more slip is required in deeper subfaults in order to produce a comparable GPS signal. The weights decay by approximately $1/r^2$ with depth (Figure 3

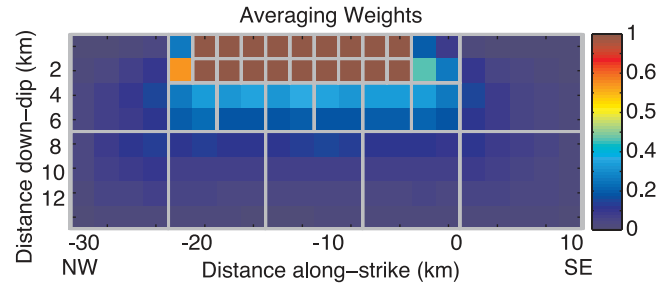


Figure 3. Map of the weights used in the w average of the slip amplitude in the second step of the inversion (seismic inversion). The GPS irregular subfaults are superimposed in gray. In general, deeper subfaults have smaller weights (weights generally decay with $1/r^2$ from the GPS network). The weights within each irregular subfault add up to approximately, but not exactly, one. The weight values are given in Table 1.

and Table 1). The weights within each irregular subfault do not add up to exactly one, which means that in this scheme moment is not necessarily conserved within each irregular subfault. The weighted average method is signal-conserving (the kinematic models inferred from the two steps generate nearly identical GPS signals). From this point onward we will refer to the weighted average of slip as described above as w -averaged.

[31] In the strong motion inversion (second step) we constrain the w -averaged slip amplitude inside each irregular GPS subfault to match the slip for that area found by inverting the GPS data, as shown in equation (2). Note that in addition to the GPS-inferred slip \tilde{x} we also have a standard deviation in this slip derived from a Monte Carlo sampling of GPS data errors. The slip amplitude in the second step should not exceed the slip amplitude, plus or minus its error, inferred from the first step. This relaxed condition takes into account the uncertainty associated with the static slip distribution arising from data errors. It also takes into account the spatial resolution of the GPS data. Because the constraint uses the irregular subfaults from step one, it effectively is a weaker constraint in areas where the GPS data have less resolution. The static constraint on the second step is implemented by adding a penalty to the object function (E), which the inversion tries to minimize, if the slip amplitude bounds are not respected. Thus, the object function [*Liu et al.*, 2006] becomes

$$E(M) = \frac{1}{\sum_{d=1}^{N_d} W_d} \sum_{d=1}^{N_d} W_d \left(1 - \frac{2 \sum_{t_b}^{t_e} \dot{u}_s(t) \frac{\dot{u}_0(t)}{A_d}}{\sum_{t_b}^{t_e} \dot{u}_s^2(t) + \sum_{t_b}^{t_e} \left(\frac{\dot{u}_0(t)}{A_d} \right)^2} \right) + E_C + E_{GPS}, \quad (3)$$

where $E(M)$ is the object function corresponding to a kinematic model M , $\dot{u}_0(t)$ are the observed velocity waveforms and $\dot{u}_s(t)$ are the synthetic velocity waveforms. As in the work by *Liu et al.* [2006], each of the N_d observed waveforms is given a weight W_d and corrected by an amplification factor A_d corresponding to the station/component of waveform d . E_C serves to impose the smoothness

Table 1. Weights Used to Perform the w-Average of the Slip Amplitude Within Each Irregular Subfault in the Second Step of the Inversion (Seismic Inversion)^a

Subfault Index Along-Strike NW (1) to SE (21)	Subfault Index Downdip From Top (1) to Bottom (8)							
	1	2	3	4	5	6	7	8
1	0.0069	0.0224	0.0361	0.0358	0.0475	0.0396	0.0317	0.0165
2	0.0148	0.0472	0.0737	0.0707	0.0903	0.0726	0.0561	0.0284
3	0.0230	0.0711	0.1047	0.0948	0.1132	0.0859	0.0631	0.0309
4	0.0375	0.1114	0.1519	0.1267	0.1388	0.0983	0.0685	0.0324
5	0.2623	0.7425	0.2565	0.1924	0.1227	0.0811	0.0537	0.0246
6	1.0000	1.0000	0.3375	0.2233	0.1294	0.0808	0.0517	0.0232
7	1.0000	1.0000	0.3307	0.1902	0.1222	0.0743	0.0469	0.0208
8	1.0000	1.0000	0.3504	0.1798	0.1131	0.0682	0.0423	0.0184
9	1.0000	1.0000	0.3202	0.1757	0.1242	0.0717	0.0425	0.0179
10	1.0000	1.0000	0.3761	0.2009	0.1393	0.0781	0.0449	0.0186
11	1.0000	1.0000	0.3589	0.1882	0.1443	0.0815	0.0477	0.0201
12	1.0000	1.0000	0.3155	0.1755	0.1371	0.0806	0.0497	0.0219
13	1.0000	1.0000	0.3378	0.2044	0.1192	0.0749	0.0488	0.0223
14	1.0000	1.0000	0.3334	0.1962	0.1176	0.0761	0.0508	0.0236
15	0.1939	0.4568	0.3447	0.2161	0.1189	0.0771	0.0518	0.0243
16	0.0925	0.2686	0.2621	0.1884	0.1108	0.0741	0.0508	0.0241
17	0.0304	0.0987	0.1449	0.1194	0.1197	0.0848	0.0603	0.0293
18	0.0173	0.0590	0.0957	0.0873	0.0961	0.0727	0.0541	0.0270
19	0.0112	0.0384	0.0652	0.0637	0.0754	0.0605	0.0472	0.0243
20	0.0081	0.0274	0.0470	0.0476	0.0593	0.0498	0.0404	0.0214
21	0.0042	0.0139	0.0236	0.0243	0.0311	0.0268	0.0224	0.0121

^aThe weights are given for each subfault along the directions along strike and downdip. These weights are plotted in Figure 3.

and moment constraints [see *Liu et al.*, 2006]. In the second step of the combined inversion (constrained seismic inversion), the larger the difference between w-averaged slip inside an irregular grid and target static slip, the more the object function is penalized. Mathematically, this constraint corresponds to adding the term E_{GPS} to the object function:

$$E_{GPS} = W_{GPS} \frac{\sum_{i=1}^M |s_i^{dev}|}{M}, \quad (4)$$

$$s_i^{dev} = \begin{cases} \bar{s} - s \min, & \text{if } \bar{s} < s \min, \\ \bar{s} - s \max, & \text{if } \bar{s} > s \max, \end{cases} \quad (5)$$

where W_{GPS} is the weight given to the GPS constraint, s_i^{dev} is the amplitude of the deviation from the GPS constraint on each irregular subfault i , and M is the number of subfaults in the irregular grid used for the GPS inversion. The value s_i^{dev} is computed given \bar{s}_i , the slip amplitude w-averaged over the area of each irregular subfault i , and $s \min$, and $s \max$, the minimum and maximum slip amplitudes allowed by the GPS inversion inside each subfault. The parameters $s \max$ and $s \min$ correspond to the static slip amplitude plus or minus, respectively, its standard deviation, as inferred from the GPS inversion. The weight W_{GPS} is determined empirically keeping in mind that both the GPS constraint and the seismic data should be well fit. In the inversions we present in this paper $W_{GPS} = 0.1$. This choice of W_{GPS} leads to an increase of the final misfit by 5% due to the GPS constraint, i.e., due to the term E_{GPS} . As we will see later on, this choice of weight W_{GPS} allows for a maximum deviation of ~ 0.06 m between the final slip model and the static slip model, and still permits a very good fit to the seismic data.

[32] After performing these two steps we reach a complete description of the kinematic earthquake source, the time-space evolution of slip on the fault. The final rupture model consists of fault plane maps of the five source

parameters (slip amplitude, rake angle, rupture velocity, and accelerating and decelerating risetimes). Because the final result was obtained through a nonlinear inversion, the solution is still nonunique. Also, we are not able to mathematically compute the error in the parameters of the kinematic model. However, because we used a two-step approach, we will be able to tell which pieces of data require which features of the rupture model. Furthermore, in the combined inversion we took into account the differences in resolution wavelength of the two data sets, thus partly eradicating spurious structure from the faulting model. Finally, the comparison of 10 equally good rupture models (generated by different random sampling of the parameter space) provides a measure of the nonuniqueness of the model given fixed assumptions (fault geometry and location, velocity structure, data accuracy, etc.).

3.5. Synthetic Test

[33] In this section we test our two-step inversion algorithm by inverting synthetic data sets generated by a known faulting model. Next we will summarize the steps involved in the synthetic test:

[34] 1. We generate a synthetic rupture model, which we will refer to as the input rupture model (it will serve as input to the synthetic test) (Figure S1a in the auxiliary material).¹ This input rupture model features the same gross slip areas as the 2004 Parkfield earthquake, as inferred from previous studies [e.g., *Custódio et al.*, 2005; *Liu et al.*, 2006]. The amplitude of slip is 0.3 m close to the hypocenter and 0.2 m in the region of slip northwest of the hypocenter. The input rupture model is further characterized by a homogeneous rupture velocity of 3.0 km/s and total risetime of 0.9 s (accelerating risetime $T_1 = 0.3$ s and decelerating risetime $T_2 = 0.6$ s).

¹Auxiliary materials are available in the HTML. doi:10.1029/2008JB005746.

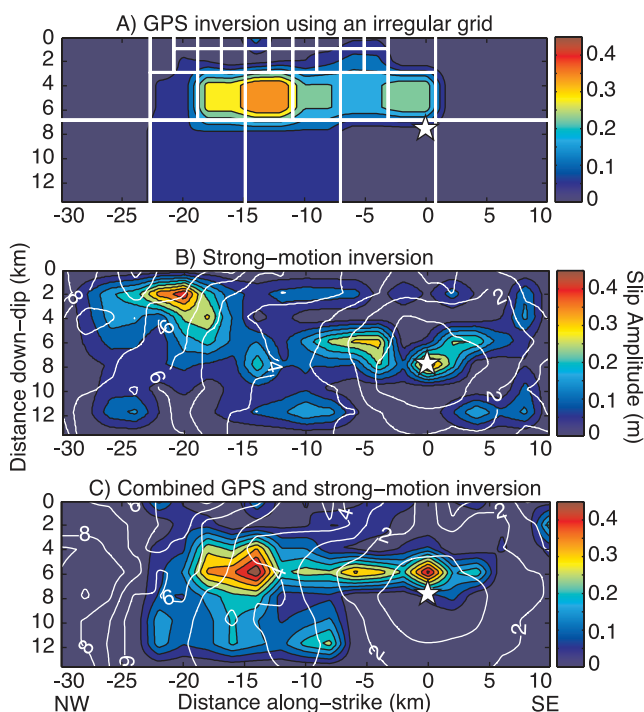


Figure 4. Slip amplitude (m) (color scale) and 1-s rupture time contours (white lines) inferred from inversion of (a) GPS data only, using an irregular grid (average of 1000 rupture models obtained through Monte Carlo error sampling), (b) strong motion data only (average of 10 rupture models obtained by different random sampling of the parameter space), and (c) two-step combined inversion (also average of 10 rupture models obtained by different random sampling of the parameter space). The white star marks the hypocenter. The irregular grid is outlined by white lines in Figure 4a.

[35] 2. On the basis of the input rupture models created in step 1 we generate GPS static data, as well as strong motion wavefield data, at the stations that recorded the 2004 Parkfield earthquake (Figures S2 and S3). We will refer to this synthetic data set as the input data set.

[36] 3. We add white noise to the input data set created above; thus we simulate more realistic Earth-like conditions where data are contaminated by noise. In the case of the GPS data set, the amplitude of the noise added is the same as that of the errors derived from the (real) GPS data processing. For the seismic data set, we arbitrarily chose the amplitude of the white noise to be 20% of the maximum amplitude in each synthetic waveform (the process of adding noise to the seismic data is the same as described by *Custódio and Archuleta* [2007]).

[37] 4. We use the two-step combined inversion algorithm described in section 3.4 to infer a rupture model (output model) from the noisy input data set created in step 3. All the tuning parameters chosen for this synthetic test (amount of smoothing, grid spacing, convergence and acceptance rate for the simulated annealing inversion, etc.) are the same as those employed in the actual inversion of the Parkfield data sets, presented in section 4.3.

[38] 5. In the first step (GPS inversion) we compute 1000 output rupture models, following the methodology pre-

sented in section 3.4. On the basis of this ensemble of output models, we infer an average slip model and corresponding standard deviation. In the second step (constrained seismic inversion) we compute 10 output rupture models. The 10 models are equally adequate, in the sense that the ground motions generated by all the models match the input synthetic records, with noise, similarly well. Our final output model is the average of the 10 preferred models (Figures S1d and S1e).

[39] Figures S2 and S3 show the fits to data resulting from this synthetic test. The data fits are very good, as expected in the case of our simple input model. The input rupture model (Figure S1a) is also well retrieved by our two-step inversion: The output rupture model (Figure S1d) is a “smeared-out” version of the input model, and in the regions of slip, maximum slip amplitude and rupture velocity are reproduced correctly. Spurious slip appears on the northwest end of the fault plane (Figure S1d); all the 10 output models yield very similar results over the rest of the fault plane (hence the minimal standard deviation, Figure S1e). While the standard deviation in this area of the fault is lower than the model error, one can see (correctly) from Figure S1e that this area of the fault has the worst resolution, and thus is most prone to spurious slip. This spurious structure could easily be eliminated by setting slip to zero on the northwest boundary of the fault plane; however, we chose not to do this in the test in order to keep the same parametrization as for the inversion of the actual recorded data sets. As we will show later, in the actual inversion of Parkfield data our final model does not have slip near this edge of the fault plane.

4. Results

4.1. GPS Inversion

[40] Figure 4a shows the slip amplitude obtained by *Page et al.* [2009] from the inversion of GPS static offsets using the irregular grid. We refer the reader to the original paper for a complete analysis of this slip model and associated errors. The model indicates that most slip occurs between a depth of 4 and 8 km. The maximum slip amplitude in the GPS model is 0.3 m, and takes place 10 to 20 km northwest of the hypocenter. A second region of slip is located close to the hypocenter, where slip attains 0.2 m. Note that these slip values are not absolute, they rather represent the average slip that occurs within the subfault area. According to this model no significant shallow slip occurred during the earthquake, which agrees with field observations of minor coseismic surface faulting [*Rymer et al.*, 2006]. It should be emphasized that the GPS data have excellent resolution for most of the shallow depths. Thus, the absence of shallow slip is a well-resolved feature. The error associated with this slip model, as inferred from observations, is variable in space (i.e., the error of the slip amplitude is different within each subfault), reaching a maximum of 0.055 m on the deeper parts of the fault (Figure S4). The average seismic moment M_0 based on the GPS modeling is 1.05×10^{18} N m.

4.2. Strong Motion Inversion

[41] The inversion of strong motion data indicates that slip occurred in two main regions of the fault (Figure 4b). Slip is spread laterally around the hypocenter, 5 km to the

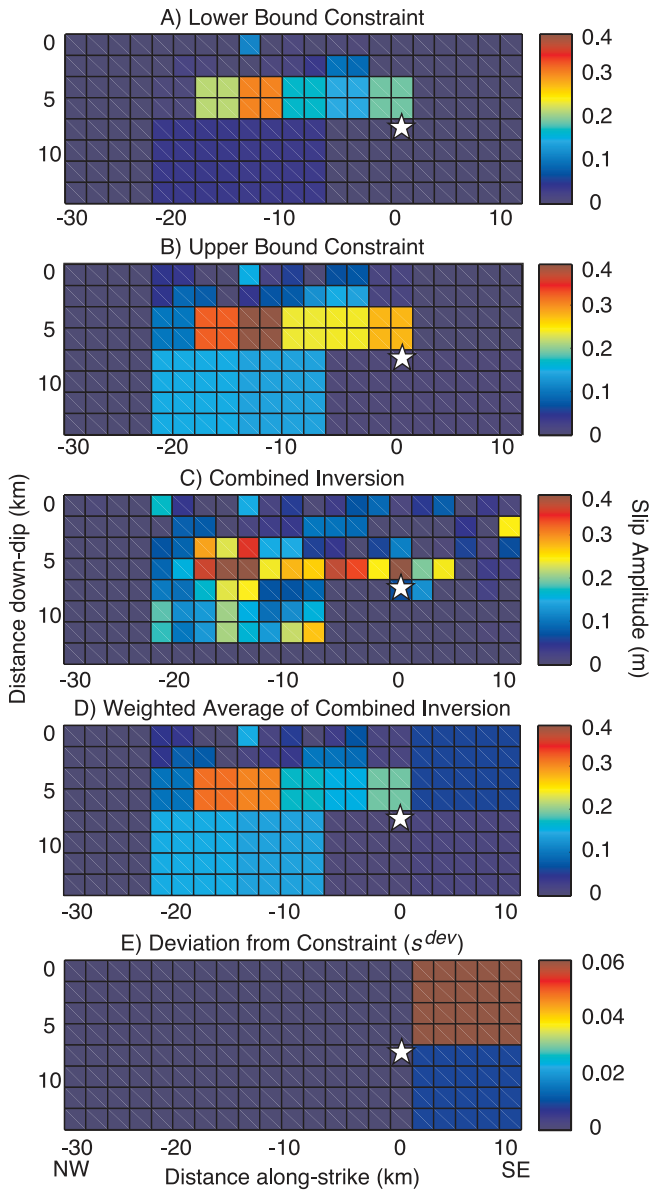


Figure 5. Slip amplitude distribution (m) obtained from the two-step combined inversion of GPS offsets and strong motion waveforms (average of 10 equally good models generated by the nonlinear inversion). (a) Minimum and (b) maximum slip amplitude slip amplitude allowed in the second step (seismic) inversion with no increase of the object function. Slip distributions in Figures 5a and 5b are obtained by subtracting and adding, respectively, the standard deviation of the static slip amplitude from its average [Page *et al.*, 2009]. (c) Result of the combined inversion. (d) The w-average of the combined inversion on the GPS irregular grid. (e) Difference between combined slip model and constraint bounds (s^{dev}). The white star marks the hypocenter.

northwest and 5 km to the southeast, and in a wider region 15 to 25 km northwest of the hypocenter, at a depth of 1–8 km. The maximum slip amplitude imaged by the strong motion data is 0.4 m with a standard deviation (inferred from

the nonuniqueness of the inversion) of 0.14 m (Figure S5). Again, the maximum slip amplitude is not a robust feature as it depends on the subfault size. The standard deviation of the slip amplitude is maximum at the hypocenter, indicating that the contours of this region of slip are not well resolved in our strong motion models. We can only interpret the other source parameters (rake angle, rupture velocity and risetime) in regions of the fault where the slip amplitude is substantially nonzero. Regions of the fault where the slip amplitude is zero do not radiate, and thus do not contribute to ground motion. In these areas, the inversion algorithm simply attributes any value to the remaining source parameters (the rupture velocity is somewhat constrained in regions of no slip if the rupture front needs to arrive further along the fault by a certain time). The rake angle is 180° in the regions of greater slip; that is, we find no significant rake rotation. The rupture velocity at the hypocenter is fast, as indicated by the separation between rupture time contours (Figure 4b). The average rupture velocity is especially fast to the southeast of the hypocenter, with values of 3.5 to 4.5 km/s (Figure S5). In section 5.2 we will discuss further the possibility of supershear rupture speeds close to the hypocenter. The standard deviation of the rupture velocity is 0.2–0.4 km/s in regions of significant slip. Risetimes are short, less than 1 s on average. We cannot adequately resolve risetimes shorter than 1 s because we only study waveforms in the passband 0.16–1.0 Hz. The average seismic moment M_0 inferred from the seismic data is 1.08×10^{18} N m.

4.3. Two-Step Inversion of GPS and Strong Motion Data

[42] Our final rupture model, based upon both static and wavefield data, results from a seismic inversion where the slip-amplitude distribution is constrained to reproduce the GPS model. Figures 5a and 5b show the minimum and maximum values that the slip amplitude may take in the seismic inversion with no penalty, i.e., with no increase in the object function. These lower and upper bounds for the slip amplitude correspond to the average slip distribution inferred from GPS data, plus or minus its standard deviation (Figure S4) [Page *et al.*, 2009]. The seismic inversion is performed on a regular grid; we require that the w-averaged slip amplitude inside each GPS irregular subgrid stays within the bounds determined by the GPS inversion. Figure 5c shows the slip-amplitude distribution obtained from the two-step combined inversion (average of 10 equally good models); Figure 5d shows the same slip distribution, but now w-averaged over the GPS irregular grid. Finally, Figure 5e shows s^{dev} , the difference between the w-averaged combined inversion (Figure 5d) and the imposed slip amplitude bounds (Figures 5a and 5b). The deviation from the constraint is practically zero in all subfaults except to the southeast. Slip in the southeast subfaults exceeds the imposed limits by 0.06 m at most. This deviation is required in order to fit the seismic data (in particular, to fit the data recorded at the Cholame Valley stations).

[43] Figures 6 and S6 show the complete kinematic models obtained from the two-step combined inversion of GPS and seismic data. Again, it should be noted that the source parameters are not well resolved in regions of the fault where the slip amplitude is low (no energy radiates

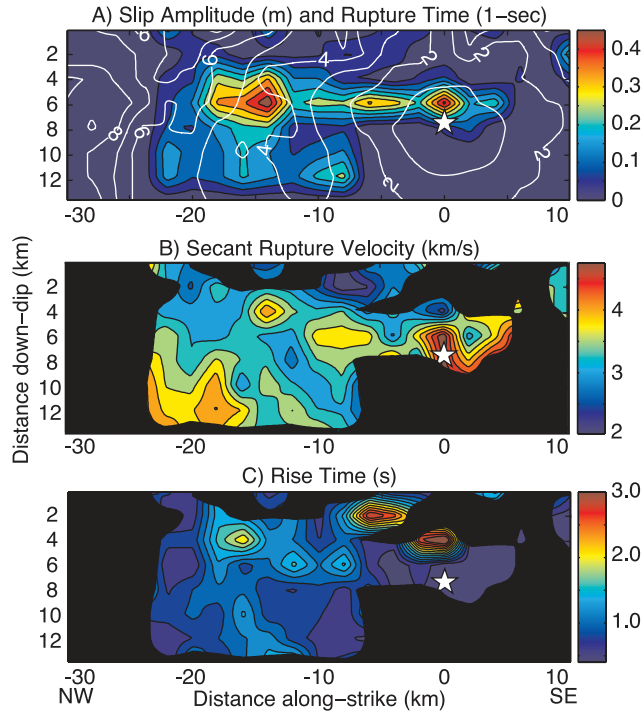


Figure 6. Complete rupture model inferred from the two-step combined inversion using an irregular grid in step one. This model is the average of 10 equally good models generated from the second step nonlinear inversion. (a) Slip amplitude in m (color scale) and 1-s rupture time contours (white lines). (b) Secant rupture velocity (km/s). (c) Risetime (s). Slip is assumed to be purely right lateral (rake angle of 180°). The white star marks the hypocenter. Regions of low slip (<0.05 m) were blacked out in the maps of rupture velocity and risetime, as these parameters are not well resolved in such regions.

from these regions, therefore their contribution to ground motion is null). In order to avoid overinterpretations of our kinematic model, we only present source parameters for regions where slip was higher than 0.05 m. The combined inversion places slip in two main regions of the fault: laterally around the hypocenter (3 km to the southeast and 8 km to the northwest) and 13–20 km northwest of the hypocenter, 4–8 km deep (Figure 6). Slip in these regions reaches 0.45 m; again this value represents an average slip over the area of the modeled subfaults. The standard deviation of the slip amplitude attains a maximum of 0.08 m in a region around 13 km northwest of the hypocenter, at a depth of 4–8 km. This region of slip is the least well resolved by the nonlinear inversion; the standard deviation indicates the magnitude of the uncertainty in the faulting model given the assumptions (i.e., this standard deviation does not take into account uncertainties in the assumptions). In this combined inversion we did not allow the rake to rotate, i.e., we assumed that slip was purely right lateral (rake angle of 180°). This assumption renders the combined inversion consistent with the GPS inversion (which also assumed that slip was strictly right lateral). In addition, the second step nonlinear inversion becomes more stable by

assuming no rake rotation. The rupture velocity is high in the hypocentral region of slip, between 3.5 and 4.5 km/s. In the region of slip northwest of the hypocenter, the rupture slows down to 3–3.5 km/s. The standard deviation of the rupture velocity is less than 0.2 km/s in regions of the fault with significant slip. Thus, rupture velocity is fairly well resolved in this two-step process. As discussed in section 4.2, we cannot adequately resolve risetimes below 1.0 s.

[44] In fact, we conducted some tests to investigate the effects of the unconstrained risetimes in the inversion. Figure S7 shows the result of two inversions: (1) where the total risetime was constrained to equal 0.9 s (accelerating risetime $T_1 = 0.3$ s and decelerating risetime $T_2 = 0.6$ s); and (2) with the total risetime constrained to equal 0.6 s (accelerating risetime $T_1 = 0.2$ s and decelerating risetime $T_2 = 0.4$ s). The two models inferred from these inversions are similar to the model obtained from the unconstrained inversion (Figure 6), both in terms of slip area, slip amplitude and rupture time. This test clearly illustrates that the faulting model resulting from our inversion does not depend on the specifics of risetimes below 1 s (and therefore no conclusions can be taken about the risetime of this earthquake other than it being less than 1 s over most of the fault plane).

[45] The average seismic moment M_0 inferred from the combined inversions is 1.06×10^{18} N m.

4.4. Fits to Ground Motion

[46] In this section we will compare the fits to ground motion obtained from the single data set inversions and from the combined geodetic-seismic inversion. In all cases we will use the synthetic ground motion generated by the single best model that we obtained (i.e., the model with smallest misfit amongst all equally good models). All equally good models produce identical synthetic ground motion, so the one best fit model represents well the set of good solutions. Figure 7 shows the observed horizontal GPS static offsets, along with the offsets predicted both by the GPS and the combined slip models. To quantify the goodness of fit between observed and synthetic static displacements, we will use the common variance reduction VR :

$$VR = \frac{(\sigma_0^2 - \sigma^2)}{\sigma_0^2}, \quad (6)$$

where

$$\sigma^2 = |\mathbf{A}\tilde{\mathbf{x}} - \mathbf{b}|^2 \quad (7)$$

and

$$\sigma_0^2 = |\mathbf{b}|^2. \quad (8)$$

The vector $\tilde{\mathbf{x}}$ is the slip solution inferred from the GPS data, \mathbf{b} is the vector containing the GPS data, and the matrix \mathbf{A} contains information on the velocity structure which is used to relate the data \mathbf{b} to the slip $\tilde{\mathbf{x}}$ on the fault. For more information on the GPS inversion, refer to Page et al. [2009]. The closer VR is to 100%, the better the fit between observed and recorded ground displacements. We obtain a

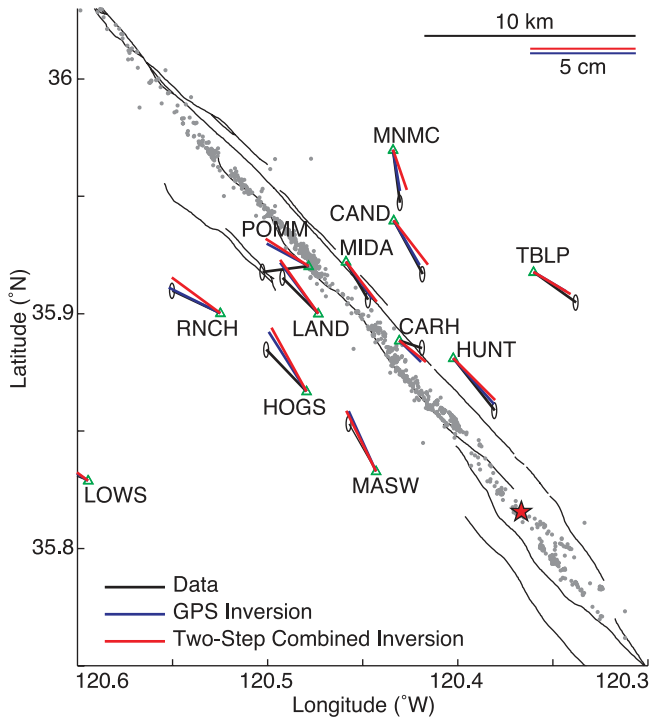


Figure 7. Horizontal GPS static offsets, observed (black), predicted by the best GPS rupture model (blue), and predicted by the best combined rupture model (red). The red star marks the epicenter. Gray dots show aftershocks locations [Thurber *et al.*, 2006].

variance reduction of 89% for the GPS-only slip model, versus 86% for the combined model. As expected, the GPS model fits the static data better than the combined model. The ground displacement recorded at station POMM is not well reproduced by our models; the ground motion at this site is difficult to reconcile with the motion at the remaining sites and may not correspond in a straightforward manner to the source dislocation (note that station POMM is located right above the fault zone). The fits to data generated by the combined and GPS model differ slightly at stations MNCM, CAND and RNCH. All of these stations are located northwest of the hypocenter and 5 km or more away from the fault plane. The discrepancy in the fits to data at these stations may be due to the deep slip identified by the combined inversion, which is absent in the GPS model. A disparity in deep slip would cause differences in the offsets predicted at some distance from the fault plane, as is the case. At all other stations, the difference in fits obtained from the GPS and the combined models is not significant. The degradation of fit to the static data in the combined inversion is negligible, but needed in order to obtain a proper fit to the strong motion data. The combined rupture model is a compromise in the fit to both data sets.

[47] Figure 8 displays observed and synthetic waveforms (predicted both by the strong motion and by the combined rupture models). Again, both sets of synthetic ground motion were generated from the best faulting model among 10 equally good models. Table 2 shows the numerical

misfits (mf) between observed $\dot{u}_0(t)$ and synthetic $\dot{u}_s(t)$ ground velocities for each waveform, as defined by a normalized correlation function:

$$mf = 1 - \frac{2 \sum_{t_b}^{t_e} \dot{u}_s(t) \frac{\dot{u}_0(t)}{A_d}}{\sum_{t_b}^{t_e} \dot{u}_s^2(t) + \sum_{t_b}^{t_e} \left(\frac{\dot{u}_0(t)}{A_d}\right)^2}. \quad (9)$$

If the misfit mf equals zero, then the synthetic waveform perfectly matches the observation; a misfit of one indicates a null correlation between the waveforms; if the signals are perfectly anticorrelated, then the misfit will be equal to one. The overall contribution arising from waveform misfits to the object function (equation (3)), which the inversion minimizes, is given by:

$$E_{\text{waveform}} = \frac{1}{\sum_{d=1}^{N_d} W_d} \sum_{d=1}^{N_d} W_d \left(1 - \frac{2 \sum_{t_b}^{t_e} \dot{u}_s(t) \frac{\dot{u}_0(t)}{A_d}}{\sum_{t_b}^{t_e} \dot{u}_s^2(t) + \sum_{t_b}^{t_e} \left(\frac{\dot{u}_0(t)}{A_d}\right)^2} \right). \quad (10)$$

This contribution (E_{waveform}) is very similar for both inversions, 0.43 for the strong motion inversion and 0.46 for the combined inversion. Most waveforms are well fit, including those that are not heavily weighted in the inversion. In particular, the vast majority of the first pulses are very well fit. Latter pulses are more difficult to match, as they often correspond to reverberations of seismic energy within the damaged fault zone. Vertical waveforms are also well fit, especially taking into account that they have very small amplitudes and are heavily downweighted in the inversion (they are downweighted by a factor of 10 in relation to the horizontal waveforms, which effectively removes them from the inversion).

[48] The GPS fit to data is more significantly degraded by the combined inversion than the seismic fit. This does not reflect a data imposition, but rather an option implemented through the weight W_{GPS} (weight of the GPS static slip constraint on the seismic inversion). In order to fit the GPS offsets better at one station, we would consistently have to abdicate from fitting a much larger number of seismic stations (five to eight stations). Because the strong motion network is denser than the geodetic network, the seismic instruments collected redundant information during the earthquake. Therefore, we felt more confident about the information that consistently appeared in several strong motion records than about information recorded at only one GPS station. For this reason, we chose to give priority to the fit of the wavefield, rather than to the fit of the static field.

5. Discussion

5.1. Combination of Different Data Sets

[49] Should we expect to obtain the same slip distribution from the inversion of different data sets? Data sets that have different resolutions are sensitive to slip that occurs over different time and length scales. Therefore, there is no reason to expect similar slip distributions to result from inversions of different data sets if the data sets have

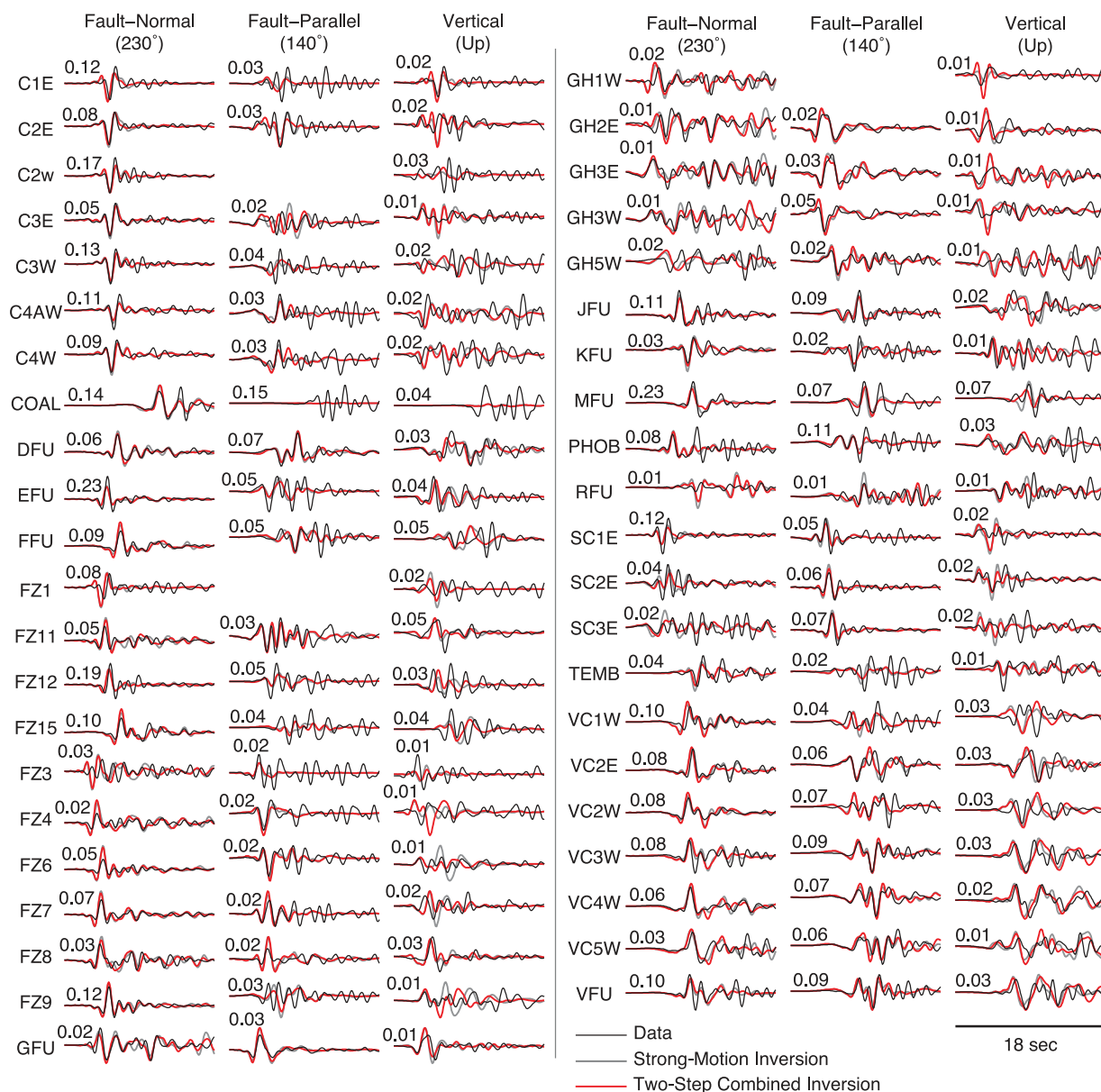


Figure 8. Strong motion velocity waveforms, fault-normal (230°), fault-parallel (140°), and vertical components of motion. Data are shown in black, synthetics generated from the best strong motion inversion are shown in gray, and synthetics of the best combined inversion are plotted in red. All waveforms are normalized in order to permit a better appreciation of the waveform fits. The maximum amplitude of each waveform is shown on its top left corner (in m/s). Station name is indicated before each row of waveforms. See Table 2 for misfit values between data and synthetics.

different resolutions. We have argued throughout this paper that in order to make sense of the slip distributions arising from different data sets, one must be able to combine all the data in a process that takes into consideration the information contained in each datum. Thus, we have built a two-step inversion following *Hernandez et al.* [1999] where each data set is inverted in a different step, and the two inversions are combined according to data resolution and error. Implicit in this method is the idea that a good fit to data does not necessarily imply a good model. Accordingly, our method may yield fits to data that are not perfect, but it attempts to limit free parameters while taking into account data error and resolution in the first step of the inversion and

the nonlinear nature of the waveform inverse problem in the second step. Next, we will examine which data require which features in our combined rupture model.

[50] All three inversions (GPS, strong motion and combined) place slip at the hypocenter, which implies that this is a region of the fault where both data sets, static and wavefield, require slip. Taking into account the different gridding systems, the three models agree fairly well upon the distribution and location of slip in this region, as well as the maximum slip amplitude. The major difference among the three models concerns slip southeast of the hypocenter. The static data do not identify slip southeast of the hypocenter, whereas the seismic data require slip there. However,

Table 2. Waveform Misfit mf Between Observed and Synthetic Ground Velocities for Each Strong Motion Station and Component of Motion^a

Station	Fault Normal (230°)		Fault Parallel (140°)		Vertical (Up)	
	SM	Comb	SM	Comb	SM	Comb
CH1E	0.39	0.46	0.83	0.96	0.50	0.33
CH2E	0.19	0.14	0.42	0.38	0.78	1.03
CH2W	0.31	0.29	–	–	1.07	1.17
CH3E	0.11	0.14	0.96	0.86	0.60	0.62
CH3W	0.25	0.26	0.96	0.84	0.95	1.06
CH4AW	0.26	0.35	0.38	0.49	1.14	1.28
CH4W	0.24	0.25	0.47	0.71	0.89	1.07
COAL	0.20	0.26	0.98	0.98	0.94	0.97
DFU	0.11	0.06	0.18	0.15	0.72	0.46
EFU	0.25	0.24	0.62	0.64	0.57	0.47
FFU	0.10	0.19	0.44	0.48	0.86	0.98
FZ1	0.70	0.80	–	–	1.12	0.97
FZ3	1.01	1.15	0.59	0.64	1.13	1.03
FZ4	0.32	0.42	0.43	0.36	0.72	1.38
FZ6	0.32	0.32	0.39	0.35	0.55	0.74
FZ7	0.21	0.20	0.40	0.43	0.82	1.06
FZ8	0.32	0.29	0.44	0.51	0.36	0.45
FZ9	0.13	0.08	1.13	1.12	0.68	0.97
FZ11	0.43	0.31	0.26	0.36	0.49	0.64
FZ12	0.38	0.43	0.69	0.74	0.94	0.82
FZ15	0.22	0.25	0.76	0.75	0.95	1.04
GFU	0.27	0.20	0.13	0.13	0.45	0.40
GH1W	0.50	0.63	–	–	0.82	0.70
GH2E	0.33	0.46	0.10	0.14	0.60	0.66
GH3E	0.23	0.19	0.15	0.23	0.59	0.51
GH3W	0.61	0.64	0.30	0.28	0.55	0.62
GH5W	0.68	0.87	0.31	0.34	0.87	0.89
JFU	0.17	0.22	0.32	0.25	0.66	0.54
KFU	0.36	0.29	0.56	0.76	0.73	0.97
MFU	0.14	0.28	0.48	0.45	0.40	0.57
PHOB	0.67	0.69	0.61	0.47	0.82	0.64
RFU	1.00	1.02	0.62	0.75	1.06	0.96
SC1E	0.31	0.41	0.43	0.41	0.85	0.77
SC2E	0.66	0.75	0.22	0.19	0.64	0.59
SC3E	0.73	0.60	0.19	0.27	0.93	0.97
TEMB	0.49	0.52	1.02	0.98	0.68	0.71
VC1W	0.45	0.43	0.78	0.76	1.45	1.62
VC2E	0.19	0.37	0.36	0.46	0.56	0.36
VC2W	0.17	0.19	0.55	0.68	0.96	0.93
VC3W	0.57	0.80	0.19	0.19	0.52	0.54
VC4W	0.14	0.24	0.24	0.32	0.47	0.35
VC5W	0.41	0.51	0.36	0.45	0.82	0.71
VFU	0.40	0.60	0.42	0.39	0.51	0.47

^aMisfits (mf , equation (9)) are shown both for the strong motion model (SM) and for the combined model (Comb). Synthetics were computed from the best of 10 equally good models.

the fit to the static data is not degraded with slip southeast of the hypocenter. Thus, we conclude that slip southeast of the hypocenter is a robust feature of our combined model that would not be imaged by the GPS data alone.

[51] All three inversions also image slip in a region 10–20 km northwest of the hypocenter; that is, both the static and wavefield data sets require slip in this region. The combined inversion eliminates the shallow slip that is present in the strong motion inversion. The absence of shallow slip in the combined rupture model allows the fit to the static offsets and does not degrade significantly the fit to the seismic data. In this case, using the two data sets led to a better control on the depth of the slip region.

[52] Overall, the maximum standard deviation in the slip amplitude is reduced from 0.12 m in the strong motion model to 0.08 m in the combined model. This corresponds

to a reduction of $\sim 30\%$ in the standard deviation of the slip amplitude. The maximum slip is unlikely to be a robust feature of the inversion. It depends upon the smoothing and grid spacing, for example. We expect robust features to have units of potency (slip \times fault area), not slip (the most robust features are the amplitudes of the vectors corresponding to high singular values, which have units of potency). The maximum standard deviation in rupture velocity is also reduced from 0.4 km/s in the strong motion model to 0.2 km/s in the combined model (in regions of significant slip). Using the static GPS data set in addition to the strong motion data reduced the uncertainty in our rupture models arising from inversion nonuniqueness. This fact is not surprising, given that the two-step inversion limits the parameter space of the strong motion inversion (second step).

5.2. Did the 2004 $M_w 6$ Parkfield Earthquake Start as a Supershear Rupture?

[53] Both the combined rupture model and the strong motion model indicate that the rupture velocity close to the hypocenter was very fast. In particular, these inversions image a supershear rupture around the hypocenter (faster than 3.6 km/s). How robust is this feature? Previous kinematic source studies [*Custódio et al., 2005; Liu et al., 2006*], as well as preliminary studies that we conducted, are not conclusive as to the existence of supershear rupture velocities during the Parkfield earthquake. Another data set that could be used to study the rupture velocity consists of ground motion recorded by a short-baseline seismic array (U.S. Geological Survey Parkfield Dense Seismograph Array, UPSAR [*Fletcher et al., 2006*]). The sources of high-frequency arrivals at UPSAR can be used to identify the rupture front, which in turn can be mapped back onto the San Andreas Fault. Using UPSAR data, *Fletcher et al. [2006]* concluded that the 2004 Parkfield earthquake propagated as a subshear rupture. However, uncertainties in the material structure lead to corresponding errors in their mapped rupture velocities. Thus, they could not definitively exclude the hypothesis of a supershear rupture close to the hypocenter. We tried to use the map of rupture velocities inferred from the UPSAR array [*Fletcher et al., 2006*] to constrain the rupture velocity in our combined inversion. We did not succeed in this attempt due to the uncertainties associated with their rupture velocities. Because we were unable to use UPSAR information to constrain the rupture velocities in our inversion, we had to find an alternative way to better assess the value of the rupture velocity at the hypocenter. Our final approach was to test whether the GPS and strong motion data require a supershear rupture in our two-step combined inversion.

[54] Figure 9 shows a rupture model obtained from a combined inversion where the rupture velocity is constrained to remain subshear everywhere on the fault (two-step inversion, using the irregular grid). Specifically, the rupture velocity is only allowed to be as high as 3.5 km/s. This subshear rupture model displays two main regions of slip-, around the hypocenter and 10 to 20 km northwest of the hypocenter. The rupture velocity is very high in both regions of slip, especially around the hypocenter. In particular, the rupture velocity is at the maximum allowable velocity in the hypocentral region. This is reflected by the

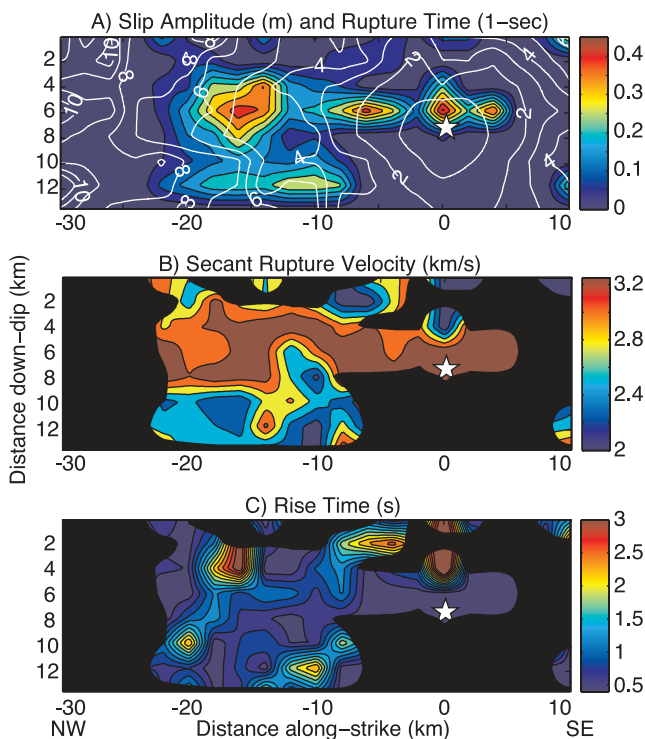


Figure 9. Complete rupture model inferred from a two-step combined inversion (using an irregular grid in the first step) where supershear rupture speeds were not allowed (rupture velocity < 3.5 km/s). (a) Slip amplitude in m (color scale) and 1-s rupture time contours (white lines). (b) Secant rupture velocity (km/s). (c) Risetime (s). The white star marks the hypocenter. Regions of low slip (< 0.05 m) were blacked out in the maps of rupture velocity and risetime, as these parameters are not well resolved in such regions.

nearly circular shape of the rupture time contours around the hypocenter. Which data require such fast rupture speed at the hypocenter? To the southeast of the hypocenter, the high rupture velocity is needed in order to fit the high-amplitude pulses of ground motion recorded at the Cholame Valley stations. A fast rupture is also required to the northwest of the hypocenter so that the next patch starts slipping at the right time, i.e., in order for the secondary pulses to arrive at the correct times at the stations. Very short risetimes (probably beyond our resolution) accompany the fast rupture velocity at the hypocenter. In a dynamic study of this earthquake, *Ma et al.* [2008] also concluded that a very fast rupture velocity was required at the hypocenter in order to fit the Cholame Valley stations (stations code starting with CH). In fact, *Ma et al.* [2008] obtain supershear rupture velocities at the hypocenter (~ 4.4 km/s) and a nearly constant subshear rupture velocity of ~ 3.0 km/s over the rest of the fault plane.

[55] In summary, we could find an appropriate rupture model with exclusively subshear velocities, although near the hypocenter the rupture velocity is equal to the shear wave velocity. In the subshear model, the slower rupture velocity at the hypocenter is compensated by a slightly larger amount of slip southeast of the hypocenter. Because the data do not require supershear speeds, we cannot affirm

that the Parkfield earthquake began as a supershear rupture. A conservative and prudent approach will be to face with skepticism the possibility of a supershear rupture velocity during the nucleation of the 2004 Parkfield earthquake. The data we analyzed cannot determine whether the 2004 Parkfield earthquake started as a supershear rupture or not. Nevertheless, a fast rupture velocity at the hypocenter is clearly demanded by the data. According to our results, this earthquake initiated with a very strong and localized burst of energy, which is attested by the confined area of slip, fast rupture velocity and short risetime at the hypocenter. Thus, the Parkfield earthquake appears to differ from other earthquakes for which slow nucleation stages have been reported [Wald *et al.*, 1991; Abercrombie and Mori, 1994; Wald *et al.*, 1996]. Such a clear behavior is not commonly inferred from kinematic source inversions and can aid in the understanding of earthquake nucleation processes.

5.3. Comparison With Other Studies

[56] In this section, we compare our combined slip model (Figure 6) with previously published models and try to understand the origin of the differences between rupture models. The models we use in the comparison are all inferred from different data sets or combinations thereof: A) GPS coseismic offsets [Murray and Langbein, 2006], B) joint use of GPS static offsets and InSAR [Johanson *et al.*, 2006], C) strong motion accelerograms [Custódio *et al.*, 2005; Liu *et al.*, 2006], and D) joint use of selected seismic and GPS data [Ji *et al.*, 2004; Bakun *et al.*, 2005].

[57] Let us start by comparing our slip distribution to those inferred from the geodetic data, model A [Murray and Langbein, 2006] and model B [Johanson *et al.*, 2006]. Both geodetic models place slip in a region 10–20 km northwest of the hypocenter, at a depth between 4 and 10 km. This slip area is also present in our combined rupture model. Furthermore, this is the region of the fault with the largest slip amplitude both in the geodetic and in our combined slip models. The values of maximum slip amplitude are different for the different models though: ~ 0.25 m in model A, ~ 0.5 m in model B, and ~ 0.45 m in our combined model. All of these values are of the same order of magnitude; the differences in the exact values may be due to different smoothing choices or different subfault sizes. We also identify a region of slip around the hypocenter. Slip in the hypocentral area is almost nonexistent in model A, but is present in model B. It is possible that model A does not image slip at the hypocenter due to the use of a regular grid (which does not take into account the decay of the GPS resolution). The hypocentral slip identified by model B is deeper (10–14 km) than in our model (6–8 km). At the time we have no good explanation for this discrepancy; it may stem from the InSAR data, which was not incorporated in our study.

[58] Next, we will examine the slip distribution inferred from strong motion data only, model C [Custódio *et al.*, 2005; Liu *et al.*, 2006]. Our combined model agrees very well with the strong motion model in the hypocentral region: slip surrounds the hypocenter laterally for a length of ~ 10 km. There is also good agreement in the value of maximum slip in this region: 0.4–0.6 m in model C, and 0.45 m in our combined model. The region of slip northwest of the hypocenter, identified in models A, B and in our

combined model, is also present in model C. Model C predicts 0.2–0.4 m of slip in this region, in accordance with our model and the geodetic inversions. Finally, model C images shallow slip 20 km northwest of the hypocenter. Practically no shallow slip exists in our combined model. In fact, the shallow slip diagnosed by model C does not allow a correct fit to the static offsets. Thus, we must conclude that the shallow slip is an artifact of model C. The strong motion model shows no significant rake rotation in regions of the fault with considerable amounts of slip. The maps of rupture velocity generated by model C and our combined model are similar, but in our combined model the rupture velocity is better established (it has a smaller standard deviation).

[59] Last, we will look at a faulting model obtained from a joint inversion of seismic and geodetic data, model D (seismic and GPS data) [Ji *et al.*, 2004; Bakun *et al.*, 2005]. Model D shows slip around the hypocenter and 10–20 km northwest of the hypocenter. The maximum slip amplitude, 1.0 m, is identified in the region northwest of the hypocenter; this value is higher than our maximum slip amplitude, which is partly a consequence of our averaging of 10 best slip models. Averaging tends to eliminate spikes in the rupture model, effectively smoothing it. Only features that are common to all 10 best models remain in the final averaged model. The shapes of the regions of slip differ between our model and the joint inversion D. We cannot fully explain this discrepancy: we can only advance that the shape of our regions of slip is to some extent a consequence of the irregular grid we use for the static inversion (step one of the combined inversion). The average rupture velocity inferred from model D is 3.0 km/s. It is not straightforward how to compare this average value to our distribution of rupture velocity. In particular, it would make no sense to simply compute the average of our map of rupture velocity, given that the rupture velocity is meaningful only in regions of the fault with considerable slip. We established that around the hypocenter the rupture velocity was very fast (≥ 3.5 km/s). In the region of slip 10–20 km northwest of the hypocenter the rupture slowed down to ~ 3.0 km/s. Our combined inversion seems to achieve a better control on rupture velocity than model D as a consequence of the data and methods employed.

5.4. Correlation Between Stress Drop and Aftershock Locations

[60] In this section, we perform a simple study of the correlation between aftershock locations and our final slip distribution (resulting from a two-step inversion, using an irregular grid for the GPS constraint, no constraint on rupture velocity, average of 10 equally good models). More advanced methods to study the correlation between aftershocks and coseismic slip distributions can be found in the literature [Woessner *et al.*, 2006]. The aftershocks of the 2004 Parkfield earthquake were located by Thurber *et al.* [2006] using the method of double differences [Waldhauser and Ellsworth, 2000; Zhang and Thurber, 2003]. Thus, the relative locations of the aftershocks within clusters are very precise but the absolute locations of the aftershocks are less so. In our analysis we consider the 2980 aftershocks that occurred during the nine months after the earthquake inside the fault plane used in our finite fault inversion. We

investigate the hypothesis that the slip distribution is correlated with the locations where aftershocks occur via the stress drop. In particular, we examine whether aftershocks occur preferentially in regions where stress increases as a consequence of coseismic slip.

[61] We compute the stress change due to slip on the fault using the finite element method of Ma and Archuleta [2006], which correctly models the bimaterial properties of the medium and free-surface effects. The calculated stress change is shown in Figure 10a. The zero stress change contour is drawn in black. Surprisingly, aftershocks tend to occur in regions of negative stress change in our model, with an average stress change of -0.97 MPa in aftershock locations. To determine the significance of this result, we generate 1000 sets of synthetic aftershocks randomly located on the modeled fault plane, and compare the average stress change at the synthetic aftershock locations to the average stress change at the true aftershock locations. We find that the negative stress drop seen at the true aftershock locations is statistically significant, as shown in Figure 10b. The red line in Figure 10b, which shows the average stress change of the real aftershock locations, is well outside of the distribution of average stress change given by randomly distributed aftershocks (the blue histogram). This test indicates that the average stress change at the true aftershock locations is far less than would be expected for random aftershock locations.

[62] One of the flaws of the test above is that it does not take into account the size of the aftershocks. If a correlation between stress change and aftershocks does indeed exist, one would expect larger aftershocks to occur in regions of larger stress increase. In order to test this hypothesis we conducted another test: we calculated the correlation coefficient between aftershock magnitude and stress change at the aftershock locations. For the true aftershock locations, the correlation is negative (Figure 10c), indicating that larger aftershocks tend to be located in regions with a smaller stress increase than smaller aftershocks. However, this finding is not statistically significant at the 95% confidence level, as it falls within the range of correlation coefficients that result from a similar analysis performed with the 1000 sets of randomly distributed aftershocks (the correlation coefficient of -0.03 is 1.4 standard deviations from the mean given by the histogram of random aftershock sets).

[63] The two tests above have weaknesses in that the results depend on regions of the fault that have no significant slip, and in addition on the boundaries of the modeled fault plane that we have chosen. In order to overcome this difficulty, we perform a final statistical test, the results of which are shown in Figure 10d. We compute an aftershock density field on the same $2 \text{ km} \times 1.95 \text{ km}$ grid used for the determination of the kinematic source parameters. Then we compute the correlation of the aftershock density field with the coseismic stress drop field, both on the same grid spacing. While this test is less sensitive both to areas with no slip and regions void of aftershocks, it does depend on the grid spacing of ~ 2 km. The results from this test are similar to those obtained in the first test, which shows that the result is robust enough not to depend on the specifics of the statistical test used. The true aftershock density is negatively correlated with stress change density, which

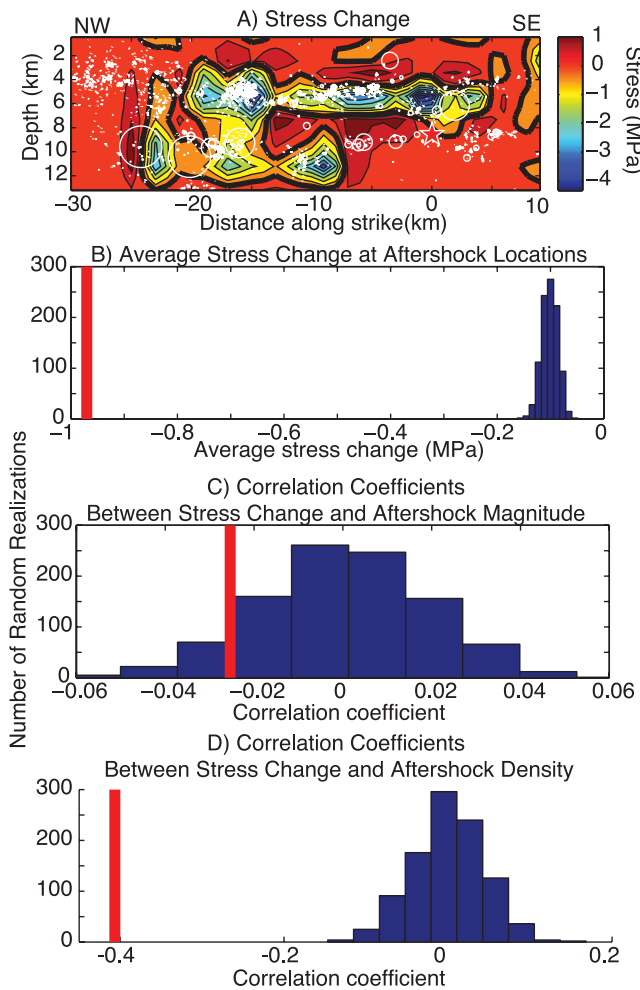


Figure 10. (a) Stress change (MPa) corresponding to the slip model inferred from the combined inversion. The black line indicates the zero stress change contour. Aftershocks are marked as white circles (the size of the circles corresponds to the area of the aftershocks assuming a circular source and a uniform stress drop of 3 MPa). The white star marks the hypocenter. (b) We generate 1000 sets of random aftershock locations. For each realization, i.e., for each set of random aftershock locations, we average the stress change over the spots where earthquakes occur. The blue histogram shows the distribution of average stress changes (in MPa) for the 1000 sets of random aftershock locations. The red bar marks the average stress change for the true aftershock distribution. (c) The blue histogram shows the distribution of correlation coefficients between stress change and aftershock magnitude for the 1000 sets of random aftershock locations. The red bar marks the correlation coefficient for the true aftershock locations. (d) This plot is identical to Figure 10c but now the correlation is performed between stress change and aftershock density.

indicates that areas of higher aftershock density tend to coincide with less stress change (in fact a negative stress change) compared to regions with few aftershocks. Again, this result is statistically significant given the standard

deviation obtained from the 1000 sets of randomly distributed aftershocks.

[64] By simple eye inspection of the slip distribution and location of aftershocks one could be tempted to state that earthquakes occur primarily on the edges of the slipped regions. However, after conducting statistical tests we find that earthquakes occur preferentially in regions where the main shock causes a *decrease* in stress (given the available aftershock locations and our kinematic slip model). This result is statistically significant and quite robust, as indicated by the two different tests we performed. In addition, even large aftershocks tend to occur in regions where our model predicts a stress drop. These results emphasize the need to actually perform quantitative tests on the relation between slip distributions and aftershocks.

[65] There are two possible explanations for our results. First, perhaps aftershocks are not in fact caused by static stress changes due to main shocks. Aftershocks could alternatively be caused by dynamic triggering [Felzer and Brodsky, 2006], or their spatial pattern could be controlled by heterogeneities in fault rheology [Waldhauser et al., 2004]. A second explanation is that either the kinematic slip pattern or the aftershock locations are not accurate enough to allow this type of test. The depth of slip in our model is somewhat dependent on the choice of grids used for the inversions. If the grids were shifted a kilometer deeper or shallower, our slip model would probably show slip at slightly different depths. Even though the strong motion data constrain the depth of slip better than GPS, it still falls off as $1/r$, so a 2-km resolution at depth is probably still optimistic. The depth of the aftershocks may also not be accurate. While the relative location of aftershocks with respect to each other has a very small error, the absolute locations still depend on the accuracy of the velocity model used. The aftershocks were located using a three-dimensional velocity structure of Parkfield, while the faulting model was inferred from a combination of two layered velocity structure. If either the true locations of all the aftershocks were shifted a couple kilometers shallower, or if the true slip had actually occurred deeper, the results of our statistical tests would be different. Also, most probably the inversion smears out the slip distribution. As a consequence, aftershocks that may actually lie in high-stress regions bordering the asperities will appear to lie in low-stress regions near the edge, but within, the asperities. Ma et al. [2008] modeled dynamically the 2004 Parkfield earthquake limiting slip to occur in the region delimited by aftershocks, between 5 and 10 km depth. Their dynamic model, with slip occurring only in the region between aftershocks, is consistent with both seismic and GPS data.

6. Conclusions

[66] We performed a source inversion for the 2004 $M_w 6$ Parkfield earthquake using both GPS static offsets and strong motion accelerograms. The GPS offsets were inferred from continuous 1-Hz displacement time series [Johnson et al., 2006]. Therefore, they are truly coseismic offsets and are not contaminated by postseismic deformation. The strong motion seismic data were integrated into velocity waveforms, filtered in the passband 0.16–1.0 Hz and corrected for site effects [Liu et al., 2006]. Our combined

inversion is a two-step procedure conceived to take into account the resolution of the GPS data set. In the first step we inverted the static field in order to obtain a map of static slip amplitude. This operation was performed on an irregular grid and using a nonnegative least squares algorithm that employed a seismic moment constraint [Page *et al.*, 2009]. We used the GPS data and its errors to infer an average slip model and a respective standard deviation. In the second step we applied a nonlinear simulated annealing inversion algorithm to the seismic data in order to obtain maps of slip amplitude, rupture velocity and risetime. This inversion has smoothness and seismic moment constraints. In this second step, the slip amplitude was constrained to resemble the static slip distribution inferred from step one. Our two-step combined inversion allows us to determine which features of the final rupture model are actually demanded by the data. Thus, even though we cannot mathematically assess the error or uniqueness of our rupture model, we can tell which components of the model are robust.

[67] The earthquake started with a very strong and localized bilateral burst of energy. Slip around the hypocenter was confined to a narrow region of slip that extended bilaterally for approximately 10 km. The maximum slip in this region reached 0.45 m. The earthquake initiated with a very fast rupture velocity (~ 3.5 km/s or more); we were not able to determine definitely whether the earthquake started as a supershear rupture. Risetimes at the hypocenter were very short, corroborating our interpretation of a strong burst of energy to start the earthquake. The rupture then proceeded to a region 10–20 km northwest of the hypocenter. This region is located near Middle Mountain and coincides with the area where the Parkfield earthquake was expected to nucleate [Bakun and McEvilly, 1984]. Slip here occurred over a wider region; its maximum amplitude was 0.45 m; the rupture velocity slowed down to approximately 3.0 km/s; and the risetimes increased to 1–2 s. Thus, our combined rupture model images two regions of the fault that displayed very different mechanical behavior during the Parkfield earthquake. The hypocentral region appears to have ruptured in a somewhat “explosive” way, whereas the region of slip northwest of the hypocenter ruptured more “gently”. It is interesting to image two close regions of a fault (separated by only ~ 5 km) behaving in such distinct ways during a moderate-size earthquake. This degree of detail in models generated from source inversions can only be obtained through very careful analysis of data sets, GPS and seismic, with complementary characteristics. Future work should address uncertainties in the Green functions, errors in the seismic data, nonuniqueness of the nonlinear seismic inversion, and uncertainties in fault location, geometry and roughness.

[68] **Acknowledgments.** We thank the California Geological Survey (CGS) and the U.S. Geological Survey (USGS) for the strong motion data used in this study. Kristine M. Larson, Kyuhong Choi, and Andria Bilich (EAR-0337206) kindly provided us the processed GPS waveforms. We are very grateful to Shuo Ma for computing the static stress drop associated with our kinematic model and for thoughtful comments and discussions. We thank two anonymous reviewers and the Associate Editor for their comments on our initial manuscript. S.C. is the recipient of a Ph.D. fellowship (SFRH/BD/14353/2003) from the Portuguese Foundation for Science and Technology. M.T.P. acknowledges the support of a LEAPS fellowship as part of an NSF GK-12 grant to UCSB. This work was

supported by the National Science Foundation (EAR-0512000, EAR-0529922, and DMR-0606092), by the Southern California Earthquake Center (SCEC), by the James S. McDonnell Foundation (grant 21002070), by the David and Lucile Packard Foundation, and by the USGS NEHRP grant 06HQGR0046. SCEC is funded by NSF Cooperative Agreement EAR-0106924 and USGS Cooperative Agreement 02HQAG0008. This is SCEC contribution 1125 and ICS contribution 0811.

References

- Abercrombie, R., and J. Mori (1994), Local observations of the onset of a large earthquake: 28 June 1992 Landers, California, *Bull. Seismol. Soc. Am.*, *84*(3), 725–734.
- Aki, K., and P. G. Richards (2002), *Quantitative Seismology*, 2nd ed., Univ. Sci. Books, Sausalito, Calif.
- Archuleta, R. J. (1984), A faulting model for the 1979 Imperial Valley earthquake, *J. Geophys. Res.*, *89*, 4559–4586.
- Bakun, W. H., and T. V. McEvilly (1984), Recurrence models and Parkfield, California, earthquakes, *J. Geophys. Res.*, *89*, 3051–3058.
- Bakun, W. H., et al. (2005), Implications for prediction and hazard assessment from the 2004 Parkfield earthquake, *Nature*, *437*(13), 969–974, doi:10.1038/nature04067.
- Ben-Zion, Y. (1998), Properties of seismic fault zone waves and their utility for imaging low-velocity structures, *J. Geophys. Res.*, *103*, 12,567–12,585, doi:10.1029/98JB00768.
- Beroza, G. C., and P. Spudich (1988), Linearized inversion for fault rupture behavior: Application to the 1984 Morgan Hill, California, earthquake, *J. Geophys. Res.*, *93*, 6275–6296.
- Borcherdt, R. D., M. J. S. Johnston, G. Glassmoyer, and C. Dietel (2006), Recordings of the 2004 Parkfield earthquake on the General Earthquake Observation System array: Implications for earthquake precursors, fault rupture, and coseismic strain changes, *Bull. Seismol. Soc. Am.*, *96*(4B), S73–S89, doi:10.1785/0120050827.
- Bouchon, M. (1997), The state of stress on some faults of the San Andreas system as inferred from near-field strong motion data, *J. Geophys. Res.*, *102*, 11,731–11,744, doi:10.1029/97JB00623.
- Choi, K., A. Bilich, K. M. Larson, and P. Axelrad (2004), Modified sidereal filtering: Implications for high-rate GPS positioning, *Geophys. Res. Lett.*, *31*, L22608, doi:10.1029/2004GL021621.
- Cohee, B. P., and G. C. Beroza (1994a), Slip distribution of the 1992 Landers earthquake and its implications for earthquake source mechanics, *Bull. Seismol. Soc. Am.*, *84*(3), 692–712.
- Cohee, B. P., and G. C. Beroza (1994b), A comparison of two methods for earthquake source inversion using strong motion seismograms, *Ann. Geophys.*, *37*, 1515–1538.
- Custódio, S., and R. J. Archuleta (2007), Parkfield earthquakes: Characteristic or complementary?, *J. Geophys. Res.*, *112*, B05310, doi:10.1029/2006JB004617.
- Custódio, S., P. Liu, and R. J. Archuleta (2005), The 2004 M_w 6.0 Parkfield, California, earthquake: Inversion of near-source ground motion using multiple data sets, *Geophys. Res. Lett.*, *32*, L23312, doi:10.1029/2005GL024417.
- Das, S., and B. V. Kostrov (1990), Inversion for seismic slip rate history and distribution with stabilizing constraints: Application to the 1986 Andreanof Islands Earthquakes, *J. Geophys. Res.*, *95*, 6899–6913.
- Das, S., and B. V. Kostrov (1994), Diversity of solutions of the problem of earthquake faulting inversion; application to SH waves for the great 1989 Macquarie Ridge earthquake, *Phys. Earth Planet. Inter.*, *85*(3–4), 293–318.
- Das, S., and P. Suhadolc (1996), On the inverse problem for earthquake rupture: The Haskell-type source model, *J. Geophys. Res.*, *101*, 5725–5738, doi:10.1029/95JB03533.
- Das, S., P. Suhadolc, and B. V. Kostrov (1996), Realistic inversions to obtain gross properties of the earthquake faulting process, *Tectonophysics*, *261*(1–3), 165–177.
- Delouis, B., D. Giardini, P. Lundgren, and J. Salichon (2002), Joint inversion of InSAR, GPS, teleseismic, and strong-motion data for the spatial and temporal distribution of earthquake slip: Application to the 1999 Izmit mainshock, *Bull. Seismol. Soc. Am.*, *92*(1), 278–299, doi:10.1785/0120000806.
- Eberhart-Phillips, D. (1989), Active faulting and deformation of the Coalinga anticline as interpreted from three-dimensional velocity structure and seismicity, *J. Geophys. Res.*, *94*, 15,565–15,586, doi:10.1029/89JB01390.
- Emolo, A., and A. Zollo (2005), Kinematic source parameters for the 1989 Loma Prieta earthquake from the nonlinear inversion of accelerograms, *Bull. Seismol. Soc. Am.*, *95*(3), 981–994, doi:10.1785/0120030193.
- Favreau, P., and R. J. Archuleta (2003), Direct seismic energy modeling and application to the 1979 Imperial Valley earthquake, *Geophys. Res. Lett.*, *30*(5), 1198, doi:10.1029/2002GL015968.

- Felzer, K. R., and E. E. Brodsky (2006), Decay of aftershock density with distance indicates triggering by dynamic stress, *Nature*, *441*, 735–738, doi:10.1038/nature04799.
- Fletcher, J. B., P. Spudich, and L. M. Baker (2006), Rupture propagation of the 2004 Parkfield, California, earthquake from observations at the UPSAR, *Bull. Seismol. Soc. Am.*, *96*(4B), S129–S142, doi:10.1785/0120050812.
- Harris, R. A., and J. R. Arrowsmith (2006), Introduction to the special issue on the 2004 Parkfield earthquake and the Parkfield earthquake prediction experiment, *Bull. Seismol. Soc. Am.*, *96*(4B), S1–S10, doi:10.1785/0120050831.
- Hartzell, S., and D. V. Helmberger (1982), Strong-motion modeling of the Imperial Valley earthquake of 1979, *Bull. Seismol. Soc. Am.*, *72*(2), 571–596.
- Hartzell, S., and S. Liu (1996), Calculation of earthquake rupture histories using a hybrid global search algorithm: application to the 1992 Landers, California, earthquake, *Phys. Earth Planet. Inter.*, *95*(1–2), 79–99.
- Hartzell, S., P. Liu, and C. Mendoza (1996), The 1994 Northridge, California, earthquake: Investigation of rupture velocity, risetime, and high-frequency radiation, *J. Geophys. Res.*, *101*, 20,091–20,108, doi:10.1029/96JB01883.
- Hartzell, S., P. Liu, C. Mendoza, C. Ji, and K. M. Larson (2007), Stability and uncertainty of finite-fault slip inversions: Application to the 2004 Parkfield, California, earthquake, *Bull. Seismol. Soc. Am.*, *97*(6), 1911–1934, doi:10.1785/0120070080.
- Hartzell, S. H., and T. H. Heaton (1983), Inversion of strong ground motion and teleseismic waveform data for the fault rupture history of the 1979 Imperial Valley, California, earthquake, *Bull. Seismol. Soc. Am.*, *73*(6A), 1553–1583.
- Henry, C., and S. Das (2002), The M_w 8.2, 17 February 1996 Biak, Indonesia, earthquake: Rupture history, aftershocks, and fault plane properties, *J. Geophys. Res.*, *107*(B11), 2312, doi:10.1029/2001JB000796.
- Hernandez, B., F. Cotton, and M. Campillo (1999), Contribution of radar interferometry to a two-step inversion of the kinematic process of the 1992 Landers earthquake, *J. Geophys. Res.*, *104*, 13,083–13,100, doi:10.1029/1999JB900078.
- Ide, S., and M. Takeo (1997), Determination of constitutive relations of fault slip based on seismic wave analysis, *J. Geophys. Res.*, *102*, 27,379–27,392, doi:10.1029/97JB02675.
- Ji, C., D. J. Wald, and D. V. Helmberger (2002a), Source description of the 1999 Hector Mine, California, earthquake, part I: Wavelet domain inversion theory and resolution analysis, *Bull. Seismol. Soc. Am.*, *92*(4), 1192–1207, doi:10.1785/0120000916.
- Ji, C., D. J. Wald, and D. V. Helmberger (2002b), Source description of the 1999 Hector Mine, California, earthquake, part II: Complexity of slip history, *Bull. Seismol. Soc. Am.*, *92*(4), 1208–1226, doi:10.1785/0120000917.
- Ji, C., K. K. Choi, N. King, K. M. Larson, and K. W. Hudnut (2004), Co-seismic slip history and early afterslip of the 2004 Parkfield earthquake, *Eos Trans. AGU*, *85*(47), Fall Meet. Suppl., Abstract S53D-04.
- Johanson, I. A., E. J. Fielding, F. Rolandone, and R. Bürgmann (2006), Coseismic and postseismic slip of the 2004 Parkfield earthquake from space-geodetic data, *Bull. Seismol. Soc. Am.*, *96*(4B), S269–S282, doi:10.1785/0120050818.
- Johnson, K. M., R. Bürgmann, and K. Larson (2006), Frictional properties on the San Andreas Fault near Parkfield, California, inferred from models of afterslip following the 2004 earthquake, *Bull. Seismol. Soc. Am.*, *96*(4B), S321–S338, doi:10.1785/0120050808.
- Konca, A. O., V. Hjørleifsdóttir, T.-R. A. Song, J.-P. Avouac, D. V. Helmberger, C. Ji, K. Sieh, R. Briggs, and A. Meltzner (2007), Rupture kinematics of the 2005 M_w 8.6 Nias-Simeulue earthquake from the joint inversion of seismic and geodetic data, *Bull. Seismol. Soc. Am.*, *97*(1A), S307–S322, doi:10.1785/0120050632.
- Langbein, J., and Y. Bock (2004), High-rate real-time GPS network at Parkfield: Utility for detecting fault slip and seismic displacements, *Geophys. Res. Lett.*, *31*, L15S20, doi:10.1029/2003GL019408.
- Langbein, J., J. R. Murray, and H. A. Snyder (2006), Co-seismic and initial post-seismic deformation from the 2004 Parkfield, California, earthquake observed by global positioning system, electronic distance meter, creepmeters, and borehole strainmeters, *Bull. Seismol. Soc. Am.*, *96*(4B), S304–S320, doi:10.1785/0120050823.
- Larson, K. M., P. Bodin, and J. Gomberg (2003), Using 1-Hz GPS data to measure deformations caused by the Denali fault earthquake, *Science*, *300*, 1421–1424, doi:10.1126/science.1084531.
- Lawson, C. L., and R. J. Hanson (1974), *Solving Least Squares Problems*, Prentice-Hall, Englewood Cliffs, N. J.
- Liu, P., and R. J. Archuleta (2004), A new nonlinear finite fault inversion with three-dimensional Greens functions: Application to the 1989 Loma Prieta, California, earthquake, *J. Geophys. Res.*, *109*, B02318, doi:10.1029/2003JB002625.
- Liu, P., S. Custódio, and R. J. Archuleta (2006), Kinematic inversion of the 2004 M_w 6.0 Parkfield earthquake including an approximation to site effects, *Bull. Seismol. Soc. Am.*, *96*(4B), S143–S158, doi:10.1785/0120050826, (Erratum, *Bull. Seismol. Soc. Am.*, *98*, 2101, 2008).
- Ma, S., and R. J. Archuleta (2006), Radiated seismic energy based on dynamic rupture models of faulting, *J. Geophys. Res.*, *111*, B05315, doi:10.1029/2005JB004055.
- Ma, S., S. Custódio, R. J. Archuleta, and P. Liu (2008), Dynamic modeling of the 2004 M_w 6.0 Parkfield, California, earthquake, *J. Geophys. Res.*, *113*, B02301, doi:10.1029/2007JB005216.
- Mai, P. M., and G. C. Beroza (2002), A spatial random field model to characterize complexity in earthquake slip, *J. Geophys. Res.*, *107*(B11), 2308, doi:10.1029/2001JB000588.
- Mikumo, T., and T. Miyatake (1995), Heterogeneous distribution of dynamic stress drop and relative fault strength recovered from the results of waveform inversion: The 1984 Morgan Hill, California, earthquake, *Bull. Seismol. Soc. Am.*, *85*(1), 178–193.
- Monelli, D., and P. M. Mai (2008), Bayesian inference of kinematic earthquake rupture parameters through fitting of strong motion data, *Geophys. J. Int.*, *173*(1), 220–232, doi:10.1111/j.1365-246X.2008.03733.x.
- Murray, J., and J. Langbein (2006), Slip on the San Andreas Fault at Parkfield, California, over two earthquake cycles and the implications for seismic hazard, *Bull. Seismol. Soc. Am.*, *96*(4B), S283–S303, doi:10.1785/0120050820.
- Nielsen, S. B., and K. B. Olsen (2000), Constraints on stress and friction from dynamic rupture models of the 1994 Northridge, California, earthquake, *Pure Appl. Geophys.*, *157*, 2029–2046.
- Olsen, K. B., R. Madariaga, and R. J. Archuleta (1997), Three-dimensional dynamic simulation of the 1992 Landers earthquake, *Science*, *278*, 834–838.
- Olson, A. H., and R. J. Apsel (1982), Finite faults and inverse theory with applications to the 1979 Imperial Valley earthquake, *Bull. Seismol. Soc. Am.*, *72*(6A), 1969–2001.
- Page, M. T., S. Custódio, R. J. Archuleta, and J. M. Carlson (2009), Constraining earthquake source inversions with GPS data: 1. Resolution based removal of artifacts, *J. Geophys. Res.*, doi:10.1029/2007JB005449, in press.
- Piatanesi, A., A. Cirella, P. Spudich, and M. Cocco (2007), A global search inversion for earthquake kinematic rupture history: Application to the 2000 western Tottori, Japan earthquake, *J. Geophys. Res.*, *112*, B07314, doi:10.1029/2006JB004821.
- Pritchard, M. E., M. Simons, P. A. Rosen, S. Hensley, and F. H. Webb (2002), Co-seismic slip from the 1995 July 30 M_w = 8.1 Antofagasta, Chile, earthquake as constrained by InSAR and GPS observations, *Geophys. J. Int.*, *150*, 362–376, doi:10.1046/j.1365-246X.2002.01661.x.
- Rymer, M. J., et al. (2006), Surface fault slip associated with the 2004 Parkfield, California, earthquake, *Bull. Seismol. Soc. Am.*, *96*(4B), S11–S27, doi:10.1785/0120050830.
- Sagiya, T., and W. Thatcher (1999), Coseismic slip resolution along a plate boundary megathrust: The Nankai Trough, southwest Japan, *J. Geophys. Res.*, *104*, 1111–1130, doi:10.1029/98JB02644.
- Sekiguchi, H., K. Irikura, and T. Iwata (2000), Fault geometry at the rupture termination of the 1995 Hyogo-ken Nanbu earthquake, *Bull. Seismol. Soc. Am.*, *90*(1), 117–133, doi:10.1785/0119990027.
- Shakal, A., V. Graizer, M. Huang, R. Borchardt, H. Haddadi, K. Lin, C. Stephens, and P. Roffers (2005), Preliminary analysis of strong-motion recordings from the 28 September 2004 Parkfield, California earthquake, *Seismol. Res. Lett.*, *76*, 27–39.
- Shakal, A., H. Haddadi, V. Graizer, K. Lin, and M. Huang (2006), Some key features of the strong-motion data from the M 6.0 Parkfield, California, earthquake of 28 September 2004, *Bull. Seismol. Soc. Am.*, *96*(4B), S90–S118, doi:10.1785/0120050817.
- Simons, M., Y. Fialko, and L. Rivera (2002), Coseismic deformation from the 1999 M_w 7.1 Hector Mine, California, earthquake as inferred from InSAR and GPS observations, *Bull. Seismol. Soc. Am.*, *92*(4), 1390–1402, doi:10.1785/0120000933.
- Somerville, P., et al. (1999), Characterizing crustal earthquake slip models for the prediction of strong ground motion, *Seismol. Res. Lett.*, *70*, 59–80.
- Thurber, C., H. Zhang, F. Waldhauser, J. Hardebeck, A. Michael, and D. Eberhart-Phillips (2006), Three-dimensional compressional wave-speed model, earthquake relocations, and focal mechanisms for the Parkfield, California, region, *Bull. Seismol. Soc. Am.*, *96*(4B), S38–S49, doi:10.1785/0120050825.
- Wald, D. J., and R. W. Graves (2001), Resolution analysis of finite fault source inversion using one- and three-dimensional Greens functions: 2. Combining seismic and geodetic data, *J. Geophys. Res.*, *106*, 8767–8788, doi:10.1029/2000JB900435.
- Wald, D. J., and T. H. Heaton (1994), Spatial and temporal distribution of slip for the 1992 Landers, California, earthquake, *Bull. Seismol. Soc. Am.*, *84*(3), 668–691.

- Wald, D. J., D. V. Helmberger, and T. H. Heaton (1991), Rupture model of the 1989 Loma Prieta earthquake from the inversion of strong-motion and broadband teleseismic data, *Bull. Seismol. Soc. Am.*, *81*(5), 1540–1572.
- Wald, D. J., T. H. Heaton, and K. W. Hudnut (1996), The slip history of the 1994 Northridge, California, earthquake determined from strong-motion, teleseismic, GPS, and leveling data, *Bull. Seismol. Soc. Am.*, *86*(1B), S49–S70.
- Waldhauser, F., and W. L. Ellsworth (2000), A double-difference earthquake location algorithm: method and application to the northern Hayward fault, California, *Bull. Seismol. Soc. Am.*, *90*(6), 1353–1368, doi:10.1785/0120000006.
- Waldhauser, F., W. L. Ellsworth, D. P. Schaff, and A. Cole (2004), Streaks, multiplets, and holes: High-resolution spatio-temporal behavior of Parkfield seismicity, *Geophys. Res. Lett.*, *31*, L18608, doi:10.1029/2004GL020649.
- Woessner, J., D. Schorlemmer, S. Wiemer, and P. M. Mai (2006), Spatial correlation of aftershock locations and on-fault main shock properties, *J. Geophys. Res.*, *111*, B08301, doi:10.1029/2005JB003961.
- Zhang, H., and C. H. Thurber (2003), Double-difference tomography: the method and its application to the Hayward fault, California, *Bull. Seismol. Soc. Am.*, *93*(5), 1875–1889, doi:10.1785/0120020190.
- Zhu, L., and L. A. Rivera (2002), A note on the dynamic and static displacements from a point source in multilayered media, *Geophys. J. Int.*, *148*, 619–627, doi:10.1046/j.1365-246X.2002.01610.x.

R. J. Archuleta, Institute for Crustal Studies, Girvetz Hall 1140, University of California, Santa Barbara, CA 93106-1100, USA. (ralph@crustal.ucsb.edu)

S. Custódio, Centro de Geofísica, Universidade de Coimbra, Avenida Dr. Dias da Silva, P-3000-134 Coimbra, Portugal. (susanacustodio@dct.uc.pt)

M. T. Page, U.S. Geological Survey, 525 South Wilson Avenue, Pasadena, CA 91106-3212, USA. (pagem@caltech.edu)